Chapter 3
Mathematical Models for GPS Positioning

In this chapter, Sect. 3.1 provides a brief introduction to the Global Positioning System (GPS). Next, Sects. 3.2 and 3.3 describe the mathematical models for GPS absolute and relative positioning, respectively. The mathematical models of GPS observations consist of a functional and a stochastic component. In contrast to the continuously improved functional model, the stochastic model characterising the statistical properties of GPS measurements is still a controversial research topic. Here the functional model is discussed with a special focus on the error sources considerably affecting GPS positioning quality, while the stochastic model is presented with respect to observation weighting and correlation structure.

For a more detailed discussion on the theory and applications of GPS, there exist a variety of textbooks with different emphases. El-Rabbany (2006) offers professionals and practitioners a non-mathematical explanation of how GPS works and a wide range of its applications. A detailed description of GPS signal structure can be found, for example, in Kaplan and Hegarty (2006, Chaps. 4, 5). Textbooks such as Teunissen and Kleusberg (1998) and Xu (2007) provide a deep theoretical insight into the mathematical models for GPS data processing, while Hofmann-Wellenhof et al. (2008) introduce the theory and practice of the Global Navigation Satellite Systems (GNSS), including the American system GPS, the Russian system GLONASS, the European system Galileo, as well as additional global, regional and augmentation systems in a more generic sense. Considering the innovative characteristics, services and potential applications anticipated in the next generation of GNSS, Prasad and Ruggieri (2005) examine the advanced architectures paving the way for the future integration of different satellite-based navigation systems. Within the context of network-aided GPS positioning, Leick (2003, Chaps. 4, 8) presents a comprehensive treatment of least-squares (LS) adjustment methods and data quality control techniques using minimum constraints, reliability measures and procedures for outlier detection. By bringing the two fields of GNSS technology and environmental studies, Awange (2012) provides a simplified presentation of the concepts of GNSS and its applications to environmental monitoring.

X. Luo, *GPS Stochastic Modelling*, Springer Theses,
DOI: 10.1007/978-3-642-34836-5_3, © Springer-Verlag Berlin Heidelberg 2013

3.1 Global Positioning System

The Global Positioning System (GPS) is a satellite-based navigation system allowing the determination of the positions of observation sites on land or at sea, in the air or in space, by means of artificial satellites. It was developed by the U.S. Department of Defence in the early 1970s as the next generation replacement to the first satellite-based navigation system, TRANSIT, which made use of Doppler shift measurements in the early 1960s. Within the framework of the TIMATION (TIMe/navigATION) program instigated in 1964, two satellites, known as NTS I and II (navigation technology satellite), were launched in 1974 and 1977, respectively. These were the first satellites equipped with atomic clocks, a rubidium (Rb) and caesium (Cs) one, respectively, and as such could be considered as prototypes of the later GPS satellites. In February 1978, the first GPS satellite was successfully launched. This section briefly outlines the main characteristics of GPS, including its reference and time systems, segments, as well as signals and observations. The readers who are interested in the evolution of satellite-based navigation are referred to Guier and Weiffenbach (1997), Prasad and Ruggieri (2005, Sect. 1.2), Ashkenazi (2006), Hofmann-Wellenhof et al. (2008, Sect. 9.1) and Parkinson and Powers (2010).

3.1.1 Reference and Time Systems

The official GPS terrestrial reference system is the three-dimensional and Earth-centred World Geodetic System 1984 (WGS84), which was originally realised by the coordinates of about 1,500 terrestrial sites derived from the TRANSIT Doppler observations. Associated with the refined WGS84 (G1150, Merrigan et al. 2002), a geocentric ellipsoid of revolution is defined by semi-major axis, flattening, Earth's angular velocity and geocentric gravitational constant. With respect to ITRF2008 (International Terrestrial Reference Frame), the current WGS84 frame shows systematic differences of the order of 1 cm (Karabatić 2011, p. 12). Moreover, the WGS84 is the reference system for the GPS broadcast ephemerides (Görres 2010b).

The system time of GPS is related to the atomic time system and referenced to coordinated universal time (UTC). However, in contrast to UTC, GPS time (GPST) is not corrected to match the Earth's rotation rate. This means that while at the GPS standard epoch, i.e., 00:00:00 UTC on January 6, 1980, UTC and GPST were coincident with each other, since January 1, 2009, 00:00:00 UTC, GPST is ahead of UTC by exactly 15 s. In addition, considering the current offset of 19 s between GPST and international atomic time (TAI), it follows that

$$\mathrm{GPST} = \mathrm{UTC} + 15\,\mathrm{s} \quad \text{and} \quad \mathrm{GPST} = \mathrm{TAI} - 19\,\mathrm{s}. \tag{3.1}$$

Therefore, TAI and UTC currently differ by an integer number of 34 s. This difference will become 35 s after July 1, 2012, 00:00:00 UTC, since a positive leap second will

be introduced at the end of June 2012 (Bulletin C43-IERS 2012). The actual integer offsets are reported by the International Bureau of Weights and Measures (BIPM[1]). Starting from the Julian date (JD) of the GPS standard epoch JD_0=2444244.5, the system time of GPS in terms of GPS week (GW) and day of week (DOW) can be calculated using

$$\mathrm{GW} = \mathrm{INT}\,[(\mathrm{JD} - \mathrm{JD}_0)/7] \quad \text{and} \quad \mathrm{DOW} = \mathrm{MOD}\,[\mathrm{INT}(\mathrm{JD}{+}0.5), 7]\,, \qquad (3.2)$$

where INT and MOD are the integer and modulo operators, respectively. A DOW value of 0 means Monday, 1 means Tuesday, and so on. Taking the epoch J2012.0 (i.e., January 1, 2012, 00:00:00 UTC) as an example, where JD = 2455927.5, the GW and DOW are equal to 1,669 and 6 (Sunday), respectively (Hofmann-Wellenhof et al. 2008, pp. 25, 315).

3.1.2 GPS Segments

GPS is comprised of three segments: the space, control and user segments. The present space segment consists of nominally 24 operational satellites deployed in six evenly spaced orbital planes in near-circular orbits (i.e., an elliptical shape with a maximum eccentricity of about 0.01; El-Rabbany 2006, p. 2) with an inclination of 55° and four active satellites in each orbital plane (see Fig. 3.1a). The semi-major axis of a GPS orbit is nearly 26,560 km, indicating a satellite altitude of about 20, 200 km above the Earth's surface (Langley 1991b). The revolution period of a GPS satellite is approximately half a sidereal day, i.e., around 11 h 58 min. Hence, for the same location, the satellite configuration repeats in universal time about 4 min earlier each day (Seeber 2003, p. 213). The initial operational capability (IOC) was officially announced in December 1993, meaning that 24 satellites were available to be used for navigation. The full operational capability (FOC) was achieved in July 1995, implying that the satellite constellation was tested for operational military performance (Hofmann-Wellenhof et al. 2008, p. 310). With the full constellation geometry, the space segment provides global coverage with 4–8 simultaneously observable satellites above an elevation angle of 15° at any time of day. Decreasing the elevation mask to 5°, 12 satellites will be occasionally visible (Hofmann-Wellenhof et al. 2008, p. 323).

Since 1978, different types of GPS satellites have been launched, such as the Block I (no longer in service), Block II, Block IIA (A: advanced), Block IIR (R: replenishment), Block IIR-M (M: modernised) and Block IIF (F: follow-on) satellites. During the course of the GPS modernisation, the future generation Block III satellites will be launched in 2014 and are expected to carry GPS into 2030 and beyond. In Fig. 3.1b–f, the different generations of GPS satellites are shown. Table 3.1

[1] ftp://ftp2.bipm.org/pub/tai/scale/UTCGPSGLO/utcgpsglo10.ar

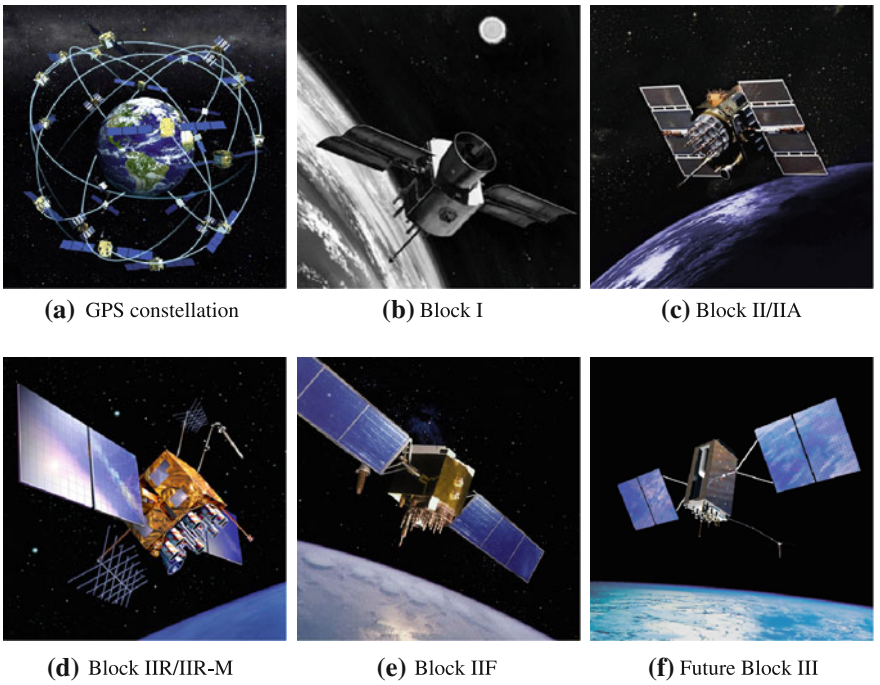

(a) GPS constellation **(b)** Block I **(c)** Block II/IIA

(d) Block IIR/IIR-M **(e)** Block IIF **(f)** Future Block III

Fig. 3.1 GPS constellation and the different generations of GPS satellites (*image sources* **a** NOAA, **b** Aerospace Corporation, **c**, **d**, **f** http://www.gps.gov, **e** http://www.navigadget.com)

Table 3.1 Selected characteristic features of the different GPS satellite categories

Satellite category	Launches during	SVN[a]	Inclination (degree)	Atomic clock	Design life (year)
Block I	1978–1985	01–11 (07)	63	1 Cs+2 Rb	4.5
Block II	1989–1990	13–21	55	2 Cs+2 Rb	7.5
Block IIA	1990–1997	22–40	55	2 Cs+2 Rb	7.5
Block IIR	1997–2004	41–61 (42)	55	3 Rb	10
Block IIR-M	2005–2009	48–58	55	3 Rb	10
Block IIF	2010–2012	62, 63, 65	55	1 Cs+2 Rb	12.7

[a] Unsuccessful launches are provided in brackets

lists some selected features of these satellite categories, where SVN denotes the satellite vehicle number (Prasad and Ruggieri 2005, pp. 6, 121).

The Block I satellites, whose orbital planes had an inclination of 63°, were built mainly for experimental purposes. Today, none of the original Block I satellites are in operation, the last being taken out of service in November 1995. Considering the 4.5 year design life of the Block I satellites, it is remarkable that some of them were operational for more than 10 years. The orbital planes of the Block II/IIA satellites are inclined at 55° to the equator. Being an advanced version of Block II,

Block IIA satellites are equipped with mutual communication capability and have a larger storage capacity, increased from 14 to 180 days. While the Block I satellite signals were fully accessible to civilian users, some Block II satellite signals are restricted in view of U.S. national security purposes. The Block IIR/IIR-M satellites are equipped with enhanced facilities for communication and intersatellite tracking. In addition, an improved antenna panel was developed for the last four Block IIR and all of the Block IIR-M satellites to increase the power of the received GPS signals.

The Block IIR-M satellites transmit the new military M-code on the carrier frequencies L1 and L2 as well as the new civil L2C-code on L2, enabling an ionospheric correction for code signals. The Block IIF satellites emit a third civil signal called L5, along with the L2C- and the M-code previously introduced into Block IIR-M. The L5 signal is expected to be more robust and to have a higher signal power level. The future Block III satellites will deliver significant improvements over the current GPS space vehicles, including a new international civil signal L1C and high-powered, anti-jamming M-code with full Earth coverage for military users. The first Block III satellite is scheduled to be launched in 2014 (Prasad and Ruggieri 2005, p. 123). For a more detailed description of the GPS satellite generations, see, for example, Prasad and Ruggieri (2005, p. 120), El-Rabbany (2006, pp. 5, 16), Hofmann-Wellenhof et al. (2008, pp. 323, 340) and Marquis and Riggs (2010). Further information about launch dates, orbital position and satellite status is available on the web site of the United States Naval Observatory (USNO, http://tycho.usno.navy.mil/gpscurr.html).

The GPS control segment is composed of a master control station (MCS) located in Colorado Springs, 12 worldwide distributed tracking (monitoring) stations and 4 ground antennas (Prasad and Ruggieri 2005, p. 123). The main tasks of the control segment are the collection of GPS observations at the unmanned tracking stations, determination and prediction of satellite orbits, clocks and other parameters at the MCS, and the uploading of navigation data to the GPS satellites. In addition, the MCS is responsible for monitoring the GPS system's integrity. During satellite maintenance or outages, the MCS sets the status of a satellite to unhealthy. Scheduled satellite maintenance or outages are reported in the so-called NANU (notice advisory to NAVSTAR users) message provided by the U.S. Coast Guard Navigation Centre (http://www.navcen.uscg.gov). For more information about the GPS control segment, the reader is referred to Prasad and Ruggieri (2005, Sects. 3.2.2, 6.3) and Hofmann-Wellenhof et al. (2008, Sect. 9.4.2).

The GPS user segment can be subdivided into three groups: (1) user categories including all military and civilian users as well as authorised and unauthorised users, (2) receiver types characterised by the type of observables and the number of tracked frequencies, depending on the application of concern, and (3) various services providing system status information and GPS products for positioning at different accuracy levels (Hofmann-Wellenhof et al. 2008, p. 7).

Table 3.2 Signal availability of the operational and future GPS satellites

Carrier	L1				L2			L5
Modulated code	C/A	P/Y	M	C	C	P/Y	M	C
Block II/IIA/IIR	X	X				X		
Block IIR-M	X	X	X		X	X	X	
Block IIF	X	X	X		X	X	X	X
Block III	X	X	X	X	X	X	X	X
Frequency [MHz]	$f_1 = 1575.42$				$f_2 = 1227.60$			$f_5 = 1176.45$
Wavelengh [cm]	$\lambda_1 = 19.0$				$\lambda_2 = 24.4$			$\lambda_5 = 25.5$

3.1.3 GPS Signals

Each GPS satellite transmits a microwave L-band radio signal composed of carrier frequencies modulated by ranging codes and a navigation message. The first operational GPS satellites (Block II, IIA and IIR) emit navigation signals on the carrier frequencies L1 and L2, while the modernised satellites (Block IIR-M, IIF and III) transmit a third civil frequency L5 and several new ranging codes on different carrier links. An overview of the GPS signals is given in Table 3.2 (Prasad and Ruggieri 2005, p. 121; Hofmann-Wellenhof et al. 2008, p. 329).

The C/A-code (C/A: coarse/acquisition), which is only modulated onto the L1 carrier, is a stream of 1023 binary digits (i.e., zeros and ones, known as bits or chips) that repeats itself every millisecond. This indicates a bit duration of approximately 1 μs and a chip length of about 300 m. The relatively short code duration allows for fast signal acquisition, but makes the C/A-code susceptible to interference. Having been designed in particular to fulfil commercial needs, the new civil L2C-code consists of the L2CM-code (M: moderate length) and a 75 times longer L2CL-code (L: long length). It shows improved cross-correlation performance and enables the correction of ionospheric effects (Fontana et al. 2001). These benefits will be available to users if the majority of the GPS satellites are L2C capable (Dixon 2005). The FOC with 24 L2C-transmitting satellites may be achieved in 2015 (Prasad and Ruggieri 2005, p. 120). To meet the requirements of safety-of-life applications, two ranging codes will be transmitted on L5, which are referred to as L5I- and L5Q-code. The L5I-code (I: in-phase) is modulated with a navigation message, while the L5Q-code (Q: quadraphase) is used as a pilot channel. In order to reduce the narrowband interference effect, both L5I and L5Q are additionally modulated with low-frequency secondary codes possessing lengths of 10 and 20 chips, respectively. The resulting codes are 10 and 20 times longer than the C/A-code and exhibit advanced autocorrelation and cross-correlation properties that allow better resistance to interference in combination with the higher signal power. A constellation of 24 L5-emitting satellites may be achieved in 2019 (Prasad and Ruggieri 2005, p. 121). The L1C-code, including a data channel L1CD and a pilot channel L1CP, will be the fourth civil signal and will provide high interoperability with Galileo's E1 signal. By applying

the multiplexing binary offset carrier (MBOC) modulation technique, more power is added to the higher frequencies to improve the tracking performance (Hein et al. 2006; Hofmann-Wellenhof et al. 2008, pp. 83, 336).

The P-code (P: precision), which is modulated onto both the L1 and L2 carriers, has been designed primarily for military purposes. It has a very long stream of about $2.35 \cdot 10^{14}$ chips and repeats itself every 38 weeks, implying a chip length of about 30 m. Due to the extremely long code length, the P-code is very difficult to directly acquire if there is no a priori information such as accurate clock corrections, coordinate estimates and satellite ephemerides. Therefore, the C/A-code is used by military receivers for a coarse acquisition, and then the receiver locks onto the P-code for higher performance. The main properties of the new military M-code modulated onto the L1 and L2 carriers are the improved anti-jamming and navigation performance, higher security using new cryptography algorithms, as well as the possibility of higher transmission power. Furthermore, being superior to the P-code, a direct acquisition of the M-code is possible (Hofmann-Wellenhof et al. 2008, pp. 333, 335).

For the initial series of GPS satellites (Block II, IIA and IIR), the navigation message is added to the P- and C/A-code, and thus is available on both the L1 and L2 carriers. It contains, along with other information, the model (a quadratic polynomial) parameters for satellite clock corrections, the satellite health status, the broadcast ephemerides, the satellite almanac and error correction data (e.g., for ionospheric effects). Of particular importance is the part known as the hand-over word (HOW) that helps the receiver achieve a rapid lock to the transmitted part of the long P-code. For the modernised GPS satellites (Block IIR-M, IIF and III), the navigation message is added to the L2CM-, L5I- and L1CD-code. A new military navigation message with efficient data structure and improved security and system integrity has been specified to be modulated onto the M-code (El-Rabbany 2006, p. 15; Hofmann-Wellenhof et al. 2008, p. 339).

Since GPS is a military system, two techniques, known as selective availability (SA) and anti-spoofing (AS), have been implemented to limit the accuracy for unauthorised users. The SA is realised by degrading the satellite clock (δ-process) and manipulating the satellite ephemerides (ϵ-process). The δ-process is carried out by dithering the fundamental frequency of the satellite clock, while the ϵ-process truncates the orbit information in the navigation message so that the satellite positions cannot be accurately determined. The effect of the δ-process can be eliminated by differencing simultaneous observations from one satellite to two receivers. The SA was activated on March 25, 1990 and turned off on May 2, 2000 (Hofmann-Wellenhof et al. 2008, pp. 319–321). Nevertheless, both processes may be retained and reactivated due to a growing awareness of the potential misuse of GPS and the increasing hybridisation of navigation approaches, which reduces the dependency on GPS as the sole navigation provider (Kelly 2006). The AS has the purpose to prevent unauthorised users from getting access to the P-code, and to "spoof" or mislead a receiver. The encrypted code is called Y-code. In doing so, adversaries could neither jam the satellite signal using ground-based transmitters, nor spoof military

GPS receivers by transmitting a false P-code from a satellite. The time periods during which the AS was activated can be found in Steigenberger (2009, p. 15).

3.1.4 GPS Observations

GPS observations include code pseudo-range measurements in the unit meter, carrier-phase measurements in the unit cycle, Doppler measurements in the unit Hertz and signal strengths in the unit decibel Hertz or in manufacturer-specific units (see Sect. 5.1). After the activation of the AS, manufacturers of dual-frequency GPS receivers have developed different methods to recover the P-code and the L2 carrier. Nowadays, most receivers apply two approaches known as cross-correlation and Z-Tracking^{TM} (Ashjaee and Lorenz 1992; Hofmann-Wellenhof et al. 2008, pp. 101, 102). Both techniques completely recover the L2 carrier, but at a degraded signal strength. The degradation is even higher when applying the cross-correlation method. The achievement of the FOC with the modernised GPS satellites (Block IIR-M, IIF and III) will make the use of these signal-recovering techniques unnecessary (El-Rabbany 2006, p. 19).

The pseudo-range derived from code observations represents a distance measure between the antenna centre of the GPS receiver and the antenna centre of the GPS satellite by determining the signal travel time in space. Since the satellite and receiver clocks are not perfectly synchronised with each other, the measured range is distorted by the clock synchronisation error, along with other effects and biases. As a rule of thumb, the precision of a code pseudo-range is about 1 % of the chip length. Accordingly, the civil C/A-code (precise P-code) has a precision of 3 m (0.3 m) (Hofmann-Wellenhof et al. 2008, p. 106).

Another way to measure the distance between receiver and satellite is to sum up the number of full carrier cycles plus the fractional part and then multiply that by the carrier wavelength (see Table 3.2). After a GPS receiver is switched on, it is capable of keeping track of phase changes, while the satellite-specific initial number of complete cycles is still unknown or ambiguous. As long as no signal loss occurs, this phase ambiguity remains unchanged over time. The GPS phase can be measured to better than 0.01 cycles, indicating a precision of about 2 mm (Hofmann-Wellenhof et al. 2008, p. 108).

The Doppler shift represents the difference between the received satellite frequency and the stable frequency emitted by the satellite. Since this difference is linearly dependent on the radial relative velocity of the satellite with respect to the receiver, it can be used to determine the receiver velocity in real time and is thus important for navigation. Furthermore, the Doppler shift contributes to integer ambiguity resolution in kinematic surveying and may be used as an additional independent observable for point positioning. For a more detailed discussion of Doppler shift and its geodetic applications, see, for example, Leick (1995, Sect. 8.3.6.1), El-Rabbany (2006, p. 24) and Hofmann-Wellenhof et al. (2008, pp. 59, 108).

3.1.5 Linear Combinations

Based on the code pseudo-range and carrier-phase measurements on two frequencies, for example, L1 and L2, linear combinations of observations can be formed which possess new preferable properties for different purposes. Taking the phase observations Φ_1 and Φ_2 in the unit meter as an example, the resulting linear combination (LC) Φ_i is defined as

$$\Phi_i = k_{1,i} \cdot \Phi_1 + k_{2,i} \cdot \Phi_2, \tag{3.3}$$

where $k_{1,i}$ and $k_{2,i}$ are real-valued coefficients (see Table 3.3). If $n^s_{R,1}$ and $n^s_{R,2}$ are the initial phase ambiguities of Φ_1 and Φ_2 relating to receiver R and satellite s, then the ambiguity term of the linear combination is

$$n^s_{R,i} = \underbrace{\frac{k_{1,i} \cdot \lambda_1}{\lambda_i}}_{\alpha_{1,i}} n^s_{R,1} + \underbrace{\frac{k_{2,i} \cdot \lambda_2}{\lambda_i}}_{\alpha_{2,i}} n^s_{R,2}, \tag{3.4}$$

where λ_1 and λ_2 can be found in Table 3.2, and λ_i is the effective wavelength of the linear combination. For $n^s_{R,i}$ to be an integer, $\alpha_{1,i}$ and $\alpha_{2,i}$ defined in Eq. (3.4) must also be integers. On the basis of $\alpha_{1,i}$ and $\alpha_{2,i}$, the coefficients $k_{1,i}$ and $k_{2,i}$ can be expressed by

$$k_{1,i} = \lambda_i \frac{\alpha_{1,i}}{\lambda_1}, \quad k_{2,i} = \lambda_i \frac{\alpha_{2,i}}{\lambda_2}. \tag{3.5}$$

This means that using $k_{1,i}$ and $k_{2,i}$ to compute a linear combination in metric units implicitly converts Φ_1 and Φ_2 into cycles by Φ_1/λ_1 and Φ_2/λ_2 before combining them. Imposing the constraint of unchanged satellite-receiver distance, i.e., $k_{1,i} + k_{2,i} = 1$ (Collins 1999), the wavelength λ_i and frequency f_i of the linear combination Φ_i can be derived using Eq. (3.5) and the generic relationship $\lambda = c/f$ as

$$\lambda_i = \frac{\lambda_1 \lambda_2}{\alpha_{2,i} \cdot \lambda_1 + \alpha_{1,i} \cdot \lambda_2}, \quad f_i = \alpha_{1,i} \cdot f_1 + \alpha_{2,i} \cdot f_2, \tag{3.6}$$

where c is the speed of light in a vacuum, and f_1 and f_2 are given in Table 3.2. Assuming that the observations on L1 and L2 are uncorrelated and have the same noise level σ_1, the noise of the linear combination is obtained by applying the variance propagation law as

$$\sigma_i = \sigma_1 \cdot \sqrt{k^2_{1,i} + k^2_{2,i}}. \tag{3.7}$$

Different linear combinations are formed in the practice of GPS data analysis, such as the wide-lane LC (LC5), the ionosphere-free LC (LC3), the geometry-free

Table 3.3 Commonly used phase linear combinations based on L1 and L2

LC	$k_{1,i}$	$k_{2,i}$	$\alpha_{1,i}$	$\alpha_{2,i}$	λ_i [m]	σ_i/σ_1	ION_i
L1	1	0	1	0	0.190	1	1
L2	0	1	0	1	0.244	1	1.65
LC5	$\frac{f_1}{f_1-f_2} = 4.53$	$\frac{-f_2}{f_1-f_2} = -3.53$	1	−1	0.862	5.74	1.28
LC3	$\frac{f_1^2}{f_1^2-f_2^2} = 2.55$	$\frac{-f_1^2}{f_1^2-f_2^2} = -1.55$	77	−60	0.006[a]	2.98	0
LC4	1	−1	−60	77	–	1.41	0.65

[a] See, e.g., Wanninger (2000, p. 15)

LC (LC4) and the Melbourne-Wübbena LC (LC6). In Table 3.3, the main properties of the commonly used phase linear combinations are summarised, where ION_i denotes the ionospheric amplification factor with respect to Φ_1 in metric units (Collins 1999; Seeber 2003, p. 263; Howind 2005, p. 24; Dach et al. 2007, p. 42; Wildt 2007, p. 61).

Due to a large wavelength of 86.2 cm, the LC5 is particularly suitable for ambiguity resolution. The LC3 has the advantage of sufficient elimination of the first-order ionospheric effect, but the disadvantages of the noise level being increased by a factor of 3 compared to L1 and the extremely small wavelength of 6 mm which makes a direct ambiguity resolution impossible (Dach et al. 2007, p. 40). Therefore, an indirect two-step ambiguity resolution strategy is employed. On the basis of the LC5, the wide-lane integer ambiguities are first determined. Next, the resolved LC5 ambiguities are introduced into an ionosphere-free (LC3) solution to evaluate the ambiguities in narrow-lane cycles with a wavelength of $c/(f_1 + f_2) \approx 11$ cm (Hofmann-Wellenhof et al. 2008, p. 112). This strategy is able to resolve ambiguities for baselines of up to several hundred kilometres (Dach et al. 2007, pp. 181, 182). Being independent of receiver and satellite clocks, and of the associated geometry (i.e., satellite orbits and site coordinates), the LC4 mainly contains the ionospheric effects and the non-integer ambiguity terms (Steigenberger 2009, p. 18). Thus, this linear combination is particularly suitable for estimating ionospheric models.

Independently described by Melbourne (1985) and Wübbena (1985), the LC6 linear combination is the difference between the carrier-phase wide-lane and the pseudo-range narrow-lane combinations (Seeber 2003, pp. 263, 265):

$$\mathrm{LC6} = \frac{1}{f_1 - f_2}(f_1\Phi_1 - f_2\Phi_2) - \frac{1}{f_1 + f_2}(f_1 P_1 + f_2 P_2). \tag{3.8}$$

It also has a wavelength of 86.2 cm and eliminates the effects of geometry, clocks, the ionosphere and the troposphere. Along with good P-code data, providing a precision of less than 1 m, the LC6 can be used to resolve the wide-lane ambiguities for very long baselines of up to 6,000 km and to check observations for cycle slips (i.e., discontinuities in the carrier-phase measurements by an integer number of cycles due to temporary interruptions of the GPS signals). In addition, the noise level of

Table 3.4 Important phase linear combinations using three frequencies [λ_i: Cocard et al. (2008); σ_i/σ_1, ION_i: Eqs. (3.9) and (3.10)]

Linear combination (LC)	$\alpha_{1,i}$	$\alpha_{2,i}$	$\alpha_{3,i}$	λ_i [m]	σ_i/σ_1	ION_i
Wide-lane region	1	0	−1	0.751	**4.93**	−1.34
(75 cm $\leq \lambda_i <$ 29.31 m)	1	−6	5	3.256	103.80	**−0.07**
	0	1	−1	5.861	33.24	−1.72
	−1	8	−7	**29.305**	1262.30	−16.52
Intermediate-lane region	1	−1	1	0.197	1.52	1.09
(19 cm $\leq \lambda_i <$ 75 cm)	1	−2	2	0.204	2.54	1.19
	0	2	−1	0.235	2.13	1.51
Narrow-lane region	4	0	−3	0.108	**2.61**	−0.01
(10 cm $\leq \lambda_i <$ 19 cm)	0	24	−23	**0.125**	16.64	0.00

the LC6 is reduced by nearly 30 % compared to that of P_1 and P_2 (Dach et al. 2007, pp. 41, 42, 182).

Considering the modernised triple-frequency GPS, the number of possible linear combinations will increase drastically. Han and Rizos (1999) proposed several three-carrier combinations with larger effective wavelengths and lower noise amplifications. Odijk (2003) derived ionosphere-free combinations for which direct integer ambiguity resolution is possible. In the case of triple-frequency, different ambiguity resolution algorithms are already available, for example, the three carrier ambiguity resolution (TCAR; Forssell et al. 1997; Vollath et al. 1998), the cascade integer resolution (CIR; Hatch et al. 2000; De Jonge et al. 2000) and the least-squares ambiguity decorrelation adjustment (LAMBDA; Teunissen 1995; Teunissen et al. 2002). Subdividing all possible phase linear combinations based on L1, L2 and L5 into a wide-lane, an intermediate-lane and a narrow-lane region, Cocard et al. (2008) performed a systematic investigation of optimum three-carrier combinations with respect to effective wavelength, noise amplification and ionospheric sensitivity. The most interesting results are summarised in Table 3.4, where the subscript 3 denotes the third frequency L5 (see Table 3.2). To calculate the phase noise factor and the first-order ionospheric scale factor in metric units, Feng (2008) provided

$$\frac{\sigma_i}{\sigma_1} = \left[\frac{(\alpha_{1,i}\cdot f_1)^2 + (\alpha_{2,i}\cdot f_2)^2 + (\alpha_{3,i}\cdot f_5)^2}{(\alpha_{1,i}\cdot f_1 + \alpha_{2,i}\cdot f_2 + \alpha_{3,i}\cdot f_5)^2}\right]^{1/2}, \tag{3.9}$$

$$\mathrm{ION}_i = \frac{f_1^2(\alpha_{1,i}/f_1 + \alpha_{2,i}/f_2 + \alpha_{3,i}/f_5)}{\alpha_{1,i}\cdot f_1 + \alpha_{2,i}\cdot f_2 + \alpha_{3,i}\cdot f_5}, \tag{3.10}$$

where the carrier-phase measurements on all three frequencies are assumed to be mutually uncorrelated and identical in variance, i.e., $\sigma_1 = \sigma_2 = \sigma_5$.

In the wide-lane region, there exists no linear combination which is completely insensitive to the ionosphere and provides an acceptably low noise amplification factor at the same time. The combination ($\alpha_{1,i} = 1, \alpha_{2,i} = 0, \alpha_{3,i} = -1$) has the

lowest phase noise factor, while $(1, -6, 5)$ is the most insensitive to the ionosphere. The extra wide-lane $(0, 1, -1)$ has been the straightforward choice in all TCAR approaches. A potentially interesting combination is $(-1, 8, -7)$, resulting in a large wavelength of 29.31 m. The intermediate-lane combinations exhibit low-noise properties and a comparable ionospheric impact as on L1. To fulfil the requirement of little ionospheric influence, narrow-lane combinations can be formed. Regarding both the noise and ionospheric amplification factors, $(4, 0, -3)$ turns out to be a promising choice. The wavelength of the triple-carrier ionosphere-free linear combination $(0, 24, -23)$ amounts to about 12.5 cm, which is significantly larger than that of the corresponding double-carrier combination $(77, -60)$ (see Table 3.3). Within the context of GNSS (GPS/Galileo/BeiDou), additional useful combinations as well as their characteristics and applications are presented in Feng (2008).

3.2 Precise Point Positioning

Relying upon the principle of trilateration (Langley 1991a), simultaneously measured distances between a GPS receiver and four satellites are needed to determine the receiver's position in a three-dimensional space, along with the receiver clock synchronisation error. In this section, the basic concept of precise point positioning (PPP) is described, including the associated mathematical models and error effects. A deeper insight into PPP can be obtained from Zumberge et al. (1997), Witchayangkoon (2000) and Bisnath and Gao (2009).

3.2.1 Introduction

Representing a modern positioning technique at the cm-level precision, PPP makes use of undifferenced dual-frequency pseudo-range and carrier-phase measurements, as well as accurate satellite orbit and clock products, provided, for example, by the International GNSS Service (IGS; Moore 2007). Thereby, the first-order ionospheric effect is eliminated by means of the ionosphere-free linear combination LC3 (see Table 3.3). Other factors limiting the achievable positioning accuracy are either estimated as additional unknown parameters (e.g., receiver clock error, tropospheric delay) or accounted for by employing available sufficiently accurate models (e.g., antenna correction models, geophysical models). The PPP technique should not be confused with the code-based single point positioning (SPP) method, which uses the navigation message and achieves a positioning accuracy at the metre level (El-Rabbany 2006, Sect. 5.1).

Due to the use of the LC3 and the fact that the non-integer receiver- and satellite-dependent uncalibrated phase delays (UPD) are absorbed by the real-valued ambiguity estimates (Geng et al. 2010), it turns out to be a difficult task in PPP to resolve integer ambiguities adequately to access the full GPS carrier-phase accuracy. As a

result, long observation periods are generally required in PPP applications. Using observations on a daily basis, static PPP is able to achieve a positioning accuracy of several millimetres (Kouba and Héroux 2001). Recent studies presented in Heßelbarth (2009) showed that hourly position estimates can reach sub-decimetre accuracy, while an observation interval of 4 h provides a positioning accuracy at the centimetre level. In addition, the incorporation of the 30 s instead of the 5 min satellite clocks and the GLONASS observations leads to improved coordinate accuracy and reduced convergence time, particularly in kinematic applications (Wanninger and Heßelbarth 2009).

Using data from a network consisting of about 100 globally and homogeneously distributed reference sites, the Jet Propulsion Laboratory (JPL) generates for commercial applications real-time products with an accuracy of 15–20 cm for orbits and 0.5 ns for clocks (http://www.gdgps.net). Benefiting from these real-time products with a sampling interval of 1 s and a latency of about 5 s, Gao and Chen (2004) showed in a static control survey that all coordinate components converge to the centimetre level within 20 min. In vehicle and airborne kinematic experiments, cm-level accuracy can be achieved after about 30 min. Moreover, the high potential of the PPP-based real-time determination of atmospheric water vapour was demonstrated. To overcome the limitations of PPP, such as long convergence time and the need for dual-frequency measurements, Wübbena et al. (2005) proposed the PPP-RTK (real time kinematic) network solution which enables the use of single-frequency receivers by providing ionospheric corrections and improves the positioning accuracy and convergence time (10–50 s) by solving integer ambiguities. Recent studies have revealed that integer ambiguity resolution in PPP is possible if the non-integer term UPD can be precisely determined based on a network of reference sites (Laurichesse and Mercier 2007; Collins 2008; Ge et al. 2008). Geng et al. (2009, 2010) found that reliable ambiguity resolution can be achieved for an observation period of 1 h. Nevertheless, over 3 h of data are still required to obtain sub-centimetre accuracy for the vertical component.

The PPP-related services can be subdivided into data, processing and positioning services. During the course of becoming a true GNSS service, the IGS will provide consistent GNSS products, in particular clock corrections with enhanced accuracy and temporal resolution (Springer and Dach 2010). As a temporary solution, Heßelbarth and Wanninger (2008) suggested an interpolation technique for clock data with poor temporal resolutions. For post-processing and near real-time applications, diverse PPP online services have become convenient tools to obtain position solutions in national or global reference frames. For example, the Canadian Spatial Reference System-PPP (CSRS-PPP) online service enables worldwide point positioning with a latency of 90 min and an accuracy of centimetre or sub-decimetre level, depending on user dynamics (Tétreault et al. 2005; Ghoddousi-Fard and Dare 2006; Mireault et al. 2008). Fuhrmann et al. (2010, Chap. 6) compared four currently available online PPP services with respect to processing strategies, parameter estimation and residual properties. Applying the so-called state-space concept (Mueller 1994; Kee 1996), different global commercial services, such as OmniSTAR introduced by the Fugro company (Heister et al. 2009, 2010), StarFire developed by John Deere and Company

(Dixon 2006) and Global Differential GPS (GDGPS) operated by JPL (Bar-Sever et al. 2004), are available for real-time PPP. Assuming optimum receiving conditions, dm-level kinematic positioning accuracy is achievable using dual-frequency receivers (Kechine et al. 2003; Dixon 2006; Heister et al. 2010). While a momentary interruption of the correction signal can be easily handled, the loss of GPS signals results in significant accuracy degradation and requires reinitialisation (Heunecke and Heister 2010).

3.2.2 Functional Model

The functional model of GPS observations formulates the mathematical relationship between the measured satellite-receiver distances and the unknown parameters such as site coordinates. For static PPP, the simplified observation equation of the LC3 measurements from receiver R and satellite j is

$$\Phi^j_{R,3} = \rho^j_R + c \cdot (\delta t_R - \delta t^j) + T^j_R + \lambda_3 \cdot B^j_{R,3} + \epsilon^j_{R,3}, \tag{3.11}$$

where

ρ^j_R : geometrical range between receiver R and satellite j in m,
c : speed of light in a vacuum in m/s,
δt_R : receiver clock offset from the GPS time in s,
δt^j : satellite clock offset from the GPS time in s,
T^j_R : tropospheric signal path delay in m,
λ_3 : wavelength of the LC3 measurement in m,
$B^j_{R,3}$: non-integer phase ambiguity of the LC3 measurement in cycles,
$\epsilon^j_{R,3}$: random noise of the LC3 measurement in m.

The range ρ^j_R represents the Euclidean distance between the three-dimensional satellite position (X^j, Y^j, Z^j) at the transmission epoch and the receiver position (X_R, Y_R, Z_R) at the reception epoch, given by

$$\rho^j_R = \sqrt{(X^j - X_R)^2 + (Y^j - Y_R)^2 + (Z^j - Z_R)^2}. \tag{3.12}$$

The tropospheric slant path delay (SPD) T^j_R can be expressed as a product of the zenith path delay (ZPD) T_R and the mapping function (MF) $m^{z_j}_R$ that relates the ZPD to the SPD at a zenith distance of z_j. Hopfield (1969) showed the possibility of separating the SPD into a predominant and well-behaved dry (d) part and a complementary and volatile wet (w) part. The dry delay term can be accurately determined on the basis of air density (Davis et al. 1985), while the wet part is very difficult to handle due to atmospheric water vapour being highly variable in time and space. According to Rothacher (1992, p. 83), the total SPD can be expressed as

$$T_R^j = T_{R,d} \cdot m_{R,d}^{z_j} + T_{R,w} \cdot m_{R,w}^{z_j}, \tag{3.13}$$

where $T_{R,d}$ is the zenith dry delay (ZDD), $T_{R,w}$ is the zenith wet delay (ZWD), and $m_{R,d}$ and $m_{R,w}$ are the associated mapping functions. Under the assumption of hydrostatic equilibrium, the ZDD can be determined at the millimetre accuracy level using ground pressure measurements and is thus considered to be known. In contrast, the ZWD must be estimated based on GPS data.

Substituting Eq. (3.13) into (3.11) and introducing satellite orbit (X^j, Y^j, Z^j) and clock (δt^j) products, for example, those provided by the IGS, Eq. (3.11) becomes

$$l_{R,3}^j = \rho_R^j + c \cdot \delta t_R + T_{R,w} \cdot m_{R,w}^{z_j} + \lambda_3 \cdot B_{R,3}^j + \epsilon_{R,3}^j. \tag{3.14}$$

The vector of unknown parameters is

$$\boldsymbol{x} = (X_R, Y_R, Z_R, \delta t_R, T_{R,w}, B_{R,3}^j)^T, \quad j = 1, \ldots, n_s, \tag{3.15}$$

where n_s denotes the total number of the satellites observed by receiver R. Regarding all $l_{R,3}^j$ in Eq. (3.14) as a realisation of the vector of stochastic observables $\underline{\boldsymbol{l}}_{\boldsymbol{Z3}}$ and assuming zero-mean random measurement noise, i.e., $\mathrm{E}(\underline{\epsilon}_{R,3}^j) = 0$, the functional model of static PPP is

$$\mathrm{E}(\underline{\boldsymbol{l}}_{\boldsymbol{Z3}}) = \mathbf{F}(\boldsymbol{x}) = \rho_R^j + c \cdot \delta t_R + T_{R,w} \cdot m_{R,w}^{z_j} + \lambda_3 \cdot B_{R,3}^j, \tag{3.16}$$

where $\mathrm{E}(\cdot)$ is the expectation operator. Obviously, Eq. (3.12) is non-linear. Therefore, a linearisation of $\mathbf{F}(\boldsymbol{x})$ using the Taylor series expansion around the a priori parameter values $\boldsymbol{x}_0$ results in

$$\mathbf{F}(\boldsymbol{x}) = \mathbf{F}(\boldsymbol{x}_0) + \frac{\partial \mathbf{F}(\boldsymbol{x})}{\partial \boldsymbol{x}}(\boldsymbol{x} - \boldsymbol{x}_0) + \cdots. \tag{3.17}$$

The linearised model of the observation equations has the matrix form

$$\boldsymbol{A} \cdot \boldsymbol{\Delta}\hat{\boldsymbol{x}} = \boldsymbol{\Delta l}_{\boldsymbol{Z3}} + \boldsymbol{v}, \tag{3.18}$$

where $\boldsymbol{A}$ is the design matrix, $\boldsymbol{\Delta}\hat{\boldsymbol{x}}$ is the estimated vector of the reduced parameters (i.e., $\boldsymbol{\Delta x} = \boldsymbol{x} - \boldsymbol{x}_0$), $\boldsymbol{\Delta l}_{\boldsymbol{Z3}}$ is the vector of reduced observations [i.e., $\boldsymbol{\Delta l}_{\boldsymbol{Z3}} = \boldsymbol{l}_{\boldsymbol{Z3}} - \mathbf{F}(\boldsymbol{x}_0)$], and $\boldsymbol{v}$ is the vector of residuals. As indicated by Eq. (3.17), the design matrix $\boldsymbol{A}$ is formed by the partial derivatives of $\mathbf{F}(\boldsymbol{x})$ with respect to the unknown parameters, i.e.,

$$\boldsymbol{A} = \left[\frac{\partial \mathbf{F}(\boldsymbol{x})}{\partial X_R}, \frac{\partial \mathbf{F}(\boldsymbol{x})}{\partial Y_R}, \frac{\partial \mathbf{F}(\boldsymbol{x})}{\partial Z_R}, \frac{\partial \mathbf{F}(\boldsymbol{x})}{\partial \delta t_R}, \frac{\partial \mathbf{F}(\boldsymbol{x})}{\partial T_{R,w}}, \frac{\partial \mathbf{F}(\boldsymbol{x})}{B_{R,3}^j} \right]_{j=1,\ldots,n_s}^{\boldsymbol{x}=\boldsymbol{x}_0}, \tag{3.19}$$

where

$$\frac{\partial \mathbf{F}(\boldsymbol{x})}{\partial X_R} = \frac{X_R - X^j}{\rho_R^j}, \quad \frac{\partial \mathbf{F}(\boldsymbol{x})}{\partial Y_R} = \frac{Y_R - Y^j}{\rho_R^j}, \quad \frac{\partial \mathbf{F}(\boldsymbol{x})}{\partial Z_R} = \frac{Z_R - Z^j}{\rho_R^j},$$
$$\frac{\partial \mathbf{F}(\boldsymbol{x})}{\partial \delta t_R} = c, \quad \frac{\partial \mathbf{F}(\boldsymbol{x})}{\partial T_{R,w}} = m_{R,w}^{z_j}, \quad \frac{\partial \mathbf{F}(\boldsymbol{x})}{\partial B_{R,3}^j} = 0 \text{ or } \lambda_3. \tag{3.20}$$

Taking the weight matrix $\boldsymbol{W_{Z3}}$ to be the inverse of the cofactor matrix $\boldsymbol{Q_{Z3}}$ of the LC3 observations, i.e., $\boldsymbol{W_{Z3}} = \boldsymbol{Q_{Z3}^{-1}}$, the best linear unbiased estimate of $\boldsymbol{\Delta x}$ is obtained by means of Eq. (2.17) as

$$\boldsymbol{\Delta \hat{x}} = \underbrace{(\boldsymbol{A}^T \boldsymbol{W_{Z3}} \boldsymbol{A})^{-1} \boldsymbol{A}^T \boldsymbol{W_{Z3}}}_{\boldsymbol{H}} \boldsymbol{\Delta l_{Z3}}. \tag{3.21}$$

The final estimate of the parameter vector $\boldsymbol{x}$ is therefore

$$\boldsymbol{\hat{x}} = \boldsymbol{x}_0 + \boldsymbol{\Delta \hat{x}}, \tag{3.22}$$

and the associated variance-covariance matrix (VCM) can be derived by applying the variance-covariance propagation law to Eq. (3.21) as

$$\boldsymbol{C_{\hat{x}\hat{x}}} = \sigma_0^2 \cdot \boldsymbol{H}\, \boldsymbol{Q_{Z3}} \boldsymbol{H}^T = \sigma_0^2 \cdot (\boldsymbol{A}^T \boldsymbol{W_{Z3}} \boldsymbol{A})^{-1}. \tag{3.23}$$

The a posteriori variance of unit weight $\hat{\sigma}_0^2$ represents an estimate of σ_0^2 and can be computed from the weighted sum of squared residuals and $(n - u)$ degrees of freedom:

$$\hat{\sigma}_0^2 = \frac{\boldsymbol{v}^T \boldsymbol{W_{Z3}} \boldsymbol{v}}{n - u}, \tag{3.24}$$

where n is the number of observations, and u is the number of unknown parameters. Using Eq. (3.18), the vector of least-squares residuals $\boldsymbol{v}$ is calculated as

$$\boldsymbol{v} = \boldsymbol{A} \cdot \boldsymbol{\Delta \hat{x}} - \boldsymbol{\Delta l_{Z3}}. \tag{3.25}$$

It is important to note that the formal VCM of the estimated unknown parameters $\boldsymbol{C_{\hat{x}\hat{x}}}$ is usually over-optimistic due to the unrealistic assumption that GPS observations are physically uncorrelated (see Sect. 3.2.4). For a more detailed discussion of the (simplified) functional model of PPP, the reader is referred to Teunissen and Kleusberg (1998, pp. 187–230), Hofmann-Wellenhof et al. (2008, pp. 166, 254), and Kouba (2009).

Table 3.5 Error effects limiting the precise point positioning (PPP) quality

Satellite-specific effects	Satellite orbit and clock products
	Satellite antenna models
	Satellite phase wind-up effect[a]
	Satellite hardware delay
Atmospheric effects	Ionospheric effects
	Tropospheric effects
Site-specific effects	Multipath effects
	Receiver antenna models
	Receiver hardware delay
Site displacement effects	Effects of the solid Earth tides
	Ocean loading displacement
	Deformation due to polar motion
	Sub-daily variations of the ERP[b]
	Atmospheric pressure loading
	Further loading displacements
Relativistic effects	Effects on the equation of motion
	Shapiro (gravitational) time delay
	Effects on satellite clocks
	Effects on receiver clocks

[a] Also known as phase polarisation effect (Steigenberger 2009, p. 35)
[b] Earth rotation parameters, i.e., pole coordinates (x_p, y_p) and UT1−UTC

3.2.3 Error Sources and Effects

Section 3.2.2 only presented the simplified functional model for point positioning using dual-frequency carrier-phase observations. To exploit the full accuracy potential of PPP, additional correction terms or models are necessary to account for the satellite-specific, atmospheric, site-specific, site displacement and relativistic effects. This section provides an overview of these error sources, with a particular focus on their influences in the measurement and solution domains. The effects to be discussed in the following text are summarised in Table 3.5.

Satellite-Specific Effects

Satellite orbit and clock products. Over the past 15 years, the precision of the IGS final orbit products has improved from about 30 cm to about 2 cm. Furthermore, the IGS rapid combined products, which are generated using fewer tracking stations and with faster delivery times (17–41 h latency), are now more precise than the best analysis centre's (AC) final solution. For the GPS satellites, the largest uncertainty in the orbit determination is due to the solar radiation pressure which can be considered by estimating the so-called dynamical parameters in an enhanced orbit model, for

example, the one implemented in the Bernese GPS Software 5.0 (Beutler et al. 1994; Dach et al. 2007, pp. 31, 32). Being consistent with the orbit precision, the current IGS final clock solutions are estimated to be precise at the 0.1 ns level. After removing the small biases, the satellite clocks produced by different AC agree with standard deviations of 0.03–0.07 ns or 1–2 cm (http://acc.igs.org). Within the framework of the IGS Real-Time Pilot Project, real-time GNSS clock products with a precision of 0.5 ns will be available to users via Internet and other economical data streaming technologies. At the moment of writing, clock corrections for the GLONASS satellites are provided by the Information-Analytical Centre (IAC) and the European Space Operations Centre (ESOC) with a sampling interval of 5 min and 30 s, respectively. A comparison of the GLONASS clock products from both AC showed an agreement at the 0.08 ns level (Springer and Dach 2010).

Satellite antenna models. The necessity for correcting the separation between the GPS satellite centre of mass (COM) and the antenna phase centre (APC) arises from the fact that the force models for satellite orbit determination refer to the satellite COM, while the measurements are related to the APC. Starting from November 5, 2006 (GW 1400), the IGS convention applies the so-called absolute phase centre model igs05 (igs05_wwww.atx[2], wwww: GPS week of the latest update), including the satellite-specific z-offsets with an accuracy of several centimetres and the block-specific, nadir-dependent phase centre variations (PCV) with a precision at the sub-millimetre level (Schmid et al. 2007). The PCV of the individual satellites within one block type are quite similar, while large differences of up to 70 cm are present in the z-offsets within the Block II/IIA satellites. The GPS satellite-specific z-offsets vary from 0.5 to 2.65 m, and the block-specific PCV values reach up to about 1 cm (Karabatić 2011, pp. 25, 26). For the horizontal satellite antenna phase centre offsets (PCO), i.e., x- and y-offsets, the block-specific values provided by satellite manufacturers are used in igs05. In the case of PPP, the neglect of the satellite PCO may cause systematic errors of several centimetres in the horizontal components and up to 10 cm in the vertical component, whereas the non-consideration of the satellite PCV leads to a maximum error of 1 mm in the vertical component (Heßelbarth 2009).

Satellite phase wind-up effect. The phase wind-up effect occurs due to changes in the mutual orientation of the transmitting satellite and the receiving antenna. For a static receiver, its antenna remains oriented towards a fixed reference direction (usually north), while the GPS satellite antennas undergo rapid rotations of up to one revolution within less than half an hour when passing the subsolar point (the so-called noon turn with the Sun-satellite-Earth constellation) and after leaving the Earth's shadow (the so-called midnight turn with the Sun-Earth-satellite constellation). Since about 1994, most of the IGS AC employ the phase wind-up correction model proposed by Wu et al. (1993), which is only applicable to static receivers. Beyerle (2009) generalised this model for arbitrary receiver antenna orientations and pointed out the necessity of the phase wind-up correction in GPS reflectometry.

[2] ftp://igscb.jpl.nasa.gov/igscb/station/general/pcv_archive

This satellite-specific effect is significant for PPP when fixing the IGS satellite orbits and clocks, as it can reach up to one half of the wave length and result in dm-level position errors (Kouba 2009). For a detailed discussion on the theoretical background of this phenomenon, see, for example, Tetewsky and Mullen (1997). Practical correction models for the receiver phase wind-up effect during kinematic PPP are presented in Le and Tiberius (2006).

Satellite hardware delay. The hardware delays in the satellite and receiver electronics lead to non-integer ambiguities and cause biases between the code signals on L1 and L2, also known as inter-frequency biases. Since the hardware delays are fully correlated with the clock parameters, the resulting biases can only be determined in a differential way as differential code biases (DCB; Steigenberger, 2009, p. 16). The inter-frequency P1P2-DCB can be obtained from a global ionosphere analysis and vary from −5 to 8 ns for the GPS satellites. The biases between the two types of L1 code measurements, referred to as the intra-frequency P1C1-DCB, can be computed within a global clock analysis using the LC3. The magnitude of the P1C1-DCB is approximately one third of the P1P2-DCB, ranging between −2 and 2 ns. As shown in Dach et al. (2007, pp. 281, 282), the satellite-specific DCB values are rather stable over time. The inter-frequency biases play an important role in the determination of absolute ionosphere parameters from dual-frequency (raw or smoothed) code measurements (Newby 1992; Rideout and Coster 2006). The intra-frequency biases must be considered when estimating satellite clocks or solving ambiguities using code observations, for example, by means of the Melbourne-Wübbena linear combination LC6 [see Eq. (3.8); Dach et al. 2007, p. 182].

Atmospheric Effects

Ionospheric effects. Extending from an altitude of about 50 km to about 1,000 km, the ionosphere speeds up the propagation of the carrier-phase beyond the speed of light, while it slows down the PRN-code by the same amount. Since the ionosphere is a dispersive medium for microwaves, the resulting delay is frequency-dependent. More precisely, the lower the frequency is, the larger the delay will be. The ionospheric delay is proportional to the total electron content (TEC) along the GPS signal path, which in turn depends on the time of day/year, the 11 year solar cycle and the geographical location (El-Rabbany 2006, p. 53). The maximum ionospheric delay appears in the region about 10–15° north and south of the geomagnetic equator where the Earth's magnetic field is horizontal. The use of the LC3 eliminates the first-order (99.9 %) ionospheric effect reaching up to 150 m at low elevation angles during the ionospheric maximum. The second-order delay may cause a range bias of up to 4 cm at a satellite elevation angle of 10°, while the magnitude of the third-order effect is about 1–4 mm (Steigenberger 2009, p. 26). Analysing the second-order ionospheric delay, Elsobeiey and El-Rabbany (2011) showed that its effects on GPS satellite orbit and clock reach up to 2 cm and 0.067 ns (i.e., a range error of 2 cm), respectively. Moreover, the consideration of the second-order effect, along with advanced tro-

pospheric models, can improve the PPP coordinate solution by 3 mm and reduce the convergence time by 15 %. Further information about the higher-order ionospheric effects and their impact on GPS parameter estimates can be found in Bassiri and Hajj (1993), Kedar et al. (2003), Fritsche et al. (2005), Hernández-Pajares et al. (2007) and Pireaux et al. (2010).

Tropospheric effects. The troposphere is the lowest part of the Earth's atmosphere and reaches up to 20 km at the equator and 7 km at the poles. It contains about 80 % of the atmospheric mass and 99 % of the water vapour. Unlike the ionosphere, the troposphere is electrically neutral and is a non-dispersive medium for radio frequencies below 15 GHz (Hofmann-Wellenhof et al. 2008, p. 128). As a result, it delays the GPS phase and code measurements identically. The tropospheric delay is minimal at the tropospheric zenith and is equal to about 2.4 m at sea level. Subdividing the total zenith path delay (ZPD) into a dry (ZDD) and a wet (ZWD) component, the ZDD amounts to about 90 % of the ZPD and increases by a factor of 10 at an elevation angle of 5°. For more accurate weather forecasts and a better understanding of the Earth's climate system, the tropospheric wet delay has been exploited to reconstruct high-resolution atmospheric water vapour fields at global and regional scales (Bevis et al. 1992, 1994; Businger et al. 1996; Ware et al. 1997; Alber et al. 2000; Baltink et al. 2002; Troller 2004; Troller et al. 2006; Bender and Raabe 2007; Luo et al. 2007a,b, 2008b; Morland and Mätzler 2007; Bender et al. 2008, 2011a,b; Lutz 2009; Fuhrmann et al. 2010; Karabatić 2011). As can be seen from Eq. (3.13), high-quality ZDD and accurate MF are essential for a reliable ZWD determination, particularly when including low-elevation GPS data.

The ZDD derived based on pressure level data from numerical weather models (NWM) provided, for example, by the European Centre for Medium-Range Weather Forecasts (ECMWF; Woods 2006), is temporally variable and delivers a more realistic a priori mode than that obtained using the standard atmosphere (STDAMT; NOAA/NASA/USAF 1976). Steigenberger (2009, p. 23) showed cm-level biases between the ZDD computed using the STDATM and the ECMWF data, where the maximum bias of 19 cm was found in Antarctica. In the case that neither near-ground meteorological measurements nor representative weather model data are available for the GPS site, Luo et al. (2012a) proposed a height-dependent correction model for the ZDD calculated on the basis of the STDATM. By incorporating freely available regional surface meteorological data, this approach significantly reduces the mean bias in the a priori ZDD from several centimetres to about 5 mm. This correction model has been experimentally applied to regional water vapour determination using PPP (Fuhrmann et al. 2010, Sect. 8.1).

Up-to-date tropospheric mapping functions mainly have the continued fraction form proposed by Marini (1972), which was later modified by Herring (1992) and Niell (1996). The Niell mapping function (NMF; Niell 1996), derived based on radiosonde data, has the main advantage that the function value only depends on the day of year and the site location, but the disadvantages of low temporal/spatial (1 day/15° in latitude) resolution and the neglect of short-term variations of several

hours to days (Niell 2001). Furthermore, the dry NMF unrealistically assumes the same seasonal behaviour of the southern and northern hemispheres.

Recent mapping functions, such as the isobaric mapping function (IMF; Niell 2000) and the Vienna mapping function (VMF1; Boehm et al. 2006b), rely upon the NWM and have an improved temporal resolution of 6 h. The IMF inputs include the latitude and height of the station, the height of the 200 hpa pressure level and the ratio of the wet delay along a geometric path at an elevation angle of 3° to the zenith wet delay. The VMF1 was developed by direct ray tracing through the ECMWF weather model. Using the VMF1 instead of the NMF in GPS data analysis, Boehm et al. (2006b) found significant station height changes by up to 1 cm and precision improvements between 3 mm and 1 cm. Applying a spherical harmonic expansion up to degree and order 9 to the VMF1 parameters on a global grid, the global mapping function (GMF; Boehm et al. 2006a) represents an easy-to-implement and consistent version of the VMF1. Although the GMF is less accurate than the VMF1 in terms of modelling short-term variations, it provides more reliable height estimates than the NMF. For an elevation angle of 3°, biases of about 0.1 between the dry NMF and GMF are shown in Steigenberger (2009, p. 24). Together with the global pressure and temperature model (GPT; Boehm et al. 2007), the GMF is particularly applicable if the VMF1 is not implemented or the surface meteorological data are not available. In addition to the mapping functions in the form of continued fraction, Saha et al. (2010) proposed a new dry Tropo-Chi MF by modifying the analytical solution of the Chapman grazing incident (Chi) function. Using the Tropo-Chi function instead of the dry NMF or GMF, the vertical position error was reduced by up to about 1 cm in the Indian region.

If low-elevation data are included, the azimuthal asymmetry of the tropospheric delay at an observation site should be considered by additionally estimating horizontal troposphere gradients. These parameters describe a tilting of the tropospheric zenith (i.e., the direction with the minimal tropospheric delay) with respect to the geometrical zenith. For an elevation cut-off angle of 10°, Fuhrmann et al. (2010, p. 62) obtained meaningful and interpretable horizontal troposphere gradients from static PPP at a regional scale. A more detailed discussion of tropospheric gradients can be found in Meindl et al. (2004) and Dach et al. (2007, Sect. 11.4.3).

Site-Specific Effects

Multipath effects. Being a major error source of cm-level positioning, multipath effects distort the original GPS signals through interference with diffused and specularly reflected signals, primarily at the receiver antenna. The phase multipath error can reach a quarter of a cycle, that is about 4.8 cm for the L1 and 6.1 cm for the L2 carrier (Hofmann-Wellenhof et al. 2008, p. 157). However, this value may increase when using phase linear combinations, for example, the maximum multipath error for the LC3 is 21.7 cm (Wildt 2007, p. 61). The site-specific multipath effects can be subdivided into a near-field and a far-field component. Far-field effects show short-periodic properties (up to half an hour; Seeber 2003, p. 317) and can be

averaged out over a long observation period (e.g., several hours). In contrast, near-field effects have non-zero mean and exhibit long-periodic characteristics (up to several hours; Wübbena et al. 2006a). They can be determined during the course of the robot-based absolute antenna calibration (Wübbena et al. 2006b, 2011). Purely from geometry, signals received at low (high) satellite elevation angles are more susceptible to the far-field (near-field) multipath.

A straightforward option for multipath reduction is to avoid, as far as possible, reflecting objects in the vicinity of the receiver antenna. Further methods for multipath mitigation can be classified as follows: (1) antenna-based attenuation (e.g., improving the antenna gain pattern by choke rings, taking advantage of the right-handed signal polarisation and using absorbent antenna ground planes), (2) improved receiver architecture (e.g., employing the Gated Correlator, the advanced Strobe Correlator and the enhanced MEDLL[3]; Ray 2006) and (3) advanced signal and data processing (e.g., exploring signal-to-noise ratio measurements, smoothing carrier-phases and performing stacking and filtering techniques). For more information about multipath mitigation, see, for example, Dilßner (2007, Sect. 3.1.7) and Hofmann-Wellenhof et al. (2008, Sect. 5.6.3).

Receiver antenna models. For a receiver antenna, the antenna phase centre (APC) at which the GPS signal is received does not necessarily coincide with the antenna geometrical (mechanical) centre. The antenna PCO is the difference between the mean electrical APC and the antenna reference point (ARP) that is defined by the IGS convention as the intersection of the vertical antenna axis of symmetry with the bottom of the antenna. As demonstrated by Hofmann-Wellenhof et al. (2008, pp. 150, 154), the location of the mean APC is a function of the elevation cut-off angle. The deviation between the APC of an individual phase measurement and the mean APC is known as the antenna PCV, which is frequency-dependent and varies with elevation, azimuth and intensity of the observed signal. The PCO can reach up to 10 cm, while the PCV values are usually smaller than 2 cm for geodetic antennas (Zeimetz and Kuhlmann 2006). The magnitude of range errors caused by the receiver antenna PCO and PCV depends on the antenna type and is typically of the order of a few centimetres (El-Rabbany 2006, p. 50).

For unchanged receiver antennas, the effects of the PCO and PCV are essentially stable, providing the prerequisite for antenna calibration. Three major calibration methods are available: (1) relative field calibration using data collected on short baselines (Mader 1999), (2) absolute field calibration, where the GPS antenna is rotated and tilted by a high-precision robot (Wübbena et al. 2000) and (3) absolute calibration performed in an anechoic chamber (Zeimetz and Kuhlmann 2006). The relative method determines the PCO and PCV with respect to a reference antenna (e.g., AOAD/M_T choke ring antenna). Generally, PCV values down to an elevation angle of 10° are determined due to the higher noise level of low-elevation data. Allowing for an enhanced error separation and bias removal, the absolute methods

[3] Multipath estimating delay lock loop.

calibrate each antenna individually and provide elevation- and azimuth-dependent PCV down to 0°. The calibration accuracy represents the deviations between repeated calibrations using the same antenna and method, but under different observational conditions, and is better than 1 mm for elevation angles above 10° and about 1–2 mm below 10° (Zeimetz and Kuhlmann 2006; Görres 2010a). The converted robot calibration values with respect to the AOAD/M_T antenna are found to be very consistent with the relative IGS values at the 1–2 mm level (Rothacher 2001). The two absolute calibration methods agree with each other at the level of 1–2 mm (Görres et al. 2006; Zeimetz and Kuhlmann 2008). Using the IGS orbit and clock products in PPP, the applied receiver antenna models should conform to the current IGS convention (Kouba 2009).

Receiver hardware delay. By convention, the IGS precise satellite clock corrections must be consistent with the P1 and P2 observables. Since the clock analysis is performed on the basis of the LC3, each clock correction contains the ionosphere-free linear combination of the unknown P1 and P2 code biases. In order to be fully consistent with the satellite clock information, the code tracking data must be corrected depending on the receiver type with respect to the code registration, such as P1/P2 receivers observing C1, P1, P2 (e.g., Ashtech Z18, Javad, Topcon), C1/X2 cross-correlation receivers (e.g., Rogue, Trimble 4000) and C1/P2 receivers (e.g., recent Leica and Trimble receiver models). Otherwise, the receiver clock and position solutions may be degraded. It should be noted that certain GNSS receivers cannot be uniquely attributed to one of the classes mentioned above. For example, the Trimble NetR5 behaves like a C1/P2 receiver for GPS and like a P1/P2 receiver for GLONASS (Dach et al. 2007, pp. 279, 282). By an agreed convention, no P1P2-DCB corrections are applied in any IGS AC analysis. Therefore, such DCB calibrations are not necessary when using the LC3 of P1/P2 code data or when the IGS clock products are held fixed or constrained in dual frequency PPP (Kouba 2009). Nevertheless, the pseudo-range observations from C1/X2 and C1/P2 receivers must be corrected for the P1C1-DCB to achieve full consistency with P1/P2 data, or precise satellite clock information (Dach et al. 2007, p. 283).

Site Displacement Effects

Effects of the solid Earth tides. The solid Earth tides describe the elastic response of the Earth's crust to the external tide-generating potential of the Sun and the Moon. They result in permanent and periodic site displacements in the radial and transverse directions. The radial component of the permanent tidal effect amounts to about −12 cm at the poles and about 6 cm at the equator. Adding this effect to the "conventional tide-free" position (e.g., ITRF), one obtains the so-called "mean tide" position (Petit and Luzum 2010, p. 108).

The periodic site displacements which can be subdivided into long-periodic, diurnal and semi-diurnal movements are typically described by spherical harmonics in terms of the Love and Shida numbers (Mathews et al. 1997). The values of these

numbers depend on the site's latitude and the tidal frequency. According to the current IERS Conventions 2010 (Petit and Luzum 2010, p. 103), the periodic site displacement vector is computed by means of a two-step procedure. The first step considers the degree 2 and degree 3 tides using the respective nominal values of the Love and Shida numbers. For the degree 3 tides, only the Moon's contribution, causing a radial displacement of up to 1.7 mm, needs to be taken into account. The second step accounts for the frequency-dependent deviations of the Love and Shida numbers from their nominal values as well as the out-of-phase contribution from the zonal tides.

Comparing the solid Earth tide models specified in the IERS Conventions 1992 and 2003, Watson et al. (2006) found aliased annual and semi-annual signals in the time series of height differences. The signal amplitudes increase as a function of latitude, amounting to 0.4 mm at the equator and 2 mm at the geographical poles. Furthermore, mm-level differences with a dominant diurnal frequency were detected in the zenith path delay (ZPD) estimates. This indicates that the choice of the solid Earth tide model is an important issue for an accurate ZPD evaluation, and thus may contribute to the error budget in the PPP-based water vapour determination.

Ocean loading displacement. The ocean loading effects on the underlying crust originate from the ocean tides and are dominated by diurnal and semi-diurnal periods. In comparison to the solid Earth tides, the ocean tide loading is more localised and the resulting site displacements are almost one order of magnitude smaller, reaching up to several centimetres in the vertical component. In addition, the non-tidal ocean loading effect caused by varying sea surface height and changing density in the water column results in mm-level vertical site displacements for coastline stations (Karabatić 2011, p. 33; Williams and Penna 2011). For cm-level kinematic or short-term (several hours) static PPP along coastal regions, the ocean loading effects must be taken into account. When performing static PPP on a daily basis, where troposphere and clock estimates are required, ocean loading corrections must also be included, unless the station is more than 1000 km away from the nearest coastline (Kouba 2009). Otherwise, the ocean loading effects will map into the solutions for troposphere parameters and receiver clocks (Dragert et al. 2000). The neglect of ocean loading displacement may lead to station height errors of up to 5 cm (Heßelbarth 2009). In the current IERS Conventions 2010 (Petit and Luzum 2010, p. 109), the ocean loading displacement is characterised by site-dependent tidal coefficients. Since 2007, most IGS AC apply the ocean loading corrections considering the sub-daily centre of mass (COM) tidal variations when generating their orbit and clock products (Ray and Griffiths 2008; Kouba 2009). Therefore, using the IGS products in a PPP solution, the ocean loading corrections should not include the COM motion.

Deformation due to polar motion. Polar motion describes the changes in the Earth's rotation axis relative to the Earth's crust as viewed from an Earth-fixed reference system (e.g., ITRF). It also causes periodic site displacements of up to several centimetres due to the resulting variations in the Earth's centrifugal potential. Unlike the solid Earth tides and the ocean loading effects, the pole tides do not average to

nearly zero over 24 h and have predominantly Chandler (∼435 days) and annual periods (Torge 2001, p. 34). Considering the fact that the pole coordinates amount to 0.8 arcsec at most, the maximum site displacements due to polar motion can reach about 25 mm in the radial and 7 mm in the horizontal directions (Petit and Luzum 2010, p. 116). Using the second degree tidal Love and Shida numbers, most IGS AC apply the pole tide corrections when generating their orbit and clock products (Kouba 2009).

Sub-daily variations of the ERP. The sub-daily variations of the Earth rotation parameters (ERP), i.e., pole coordinates (x_p, y_p) and UT1 − UTC, are dominated by diurnal and sub-diurnal periods of ocean tide origin, and can reach up to 3 cm on the Earth's surface (Kouba 2009). Much like the ocean tide loading, the sub-daily ERP variations average out to nearly zero over a period of 24 h. Nevertheless, for short-term PPP, sub-daily ERP corrections are still required to achieve sub-centimetre positioning precision. This arises from the fact that the sub-daily ERP variations are not included in the current IERS Conventions 2010 (Petit and Luzum 2010, pp. 50, 52), while they have been considered in all IGS solutions since June 30, 1996 (Héroux and Kouba 2001). In particular, the instantaneous sub-daily ERP must be added to the tide-free IERS ERP values prior to all transformations between the ITRF and the ICRF (International Celestial Reference Frame). As Kouba (2002b) showed, an inconsistent application of the sub-daily ERP model by the IGS AC can result in significant orbit differences exceeding the 5 cm level. Moreover, the neglect of the sub-daily ERP variations in short-term PPP may introduce errors of more than 1 cm in the position, ZPD and receiver clock estimates.

Atmospheric pressure loading. The atmospheric pressure loading (APL) can be explained as the displacements of the Earth's crust due to the temporal variations in the geographic distribution of atmospheric mass. The APL can displace the positions of geodetic sites by as much as 10–25 mm vertically and one-tenth to one-third of this magnitude horizontally, particularly in the continental medium- and high-latitude regions where the largest pressure variations prevail (van Dam et al. 1994; Mangiarotti et al. 2001; Brondeel and Willems 2003; Rodrigues 2007). Like the ocean loading, the APL can also be separated into a tidal and a non-tidal part, where the non-tidal component plays a dominant role (Karabatić 2011, p. 33).

The geophysical approach for modelling the APL convolves Green's function (Farrell 1972) with a global pressure field provided by the ECMWF or by the NCEP (National Centres for Environmental Prediction) operational analyses. The ocean's response to the APL is modelled as an inverted barometer (Sun et al. 1995; Petrov and Boy 2004). This geophysical approach, however, suffers from the availability of a global pressure data set with a minimum latency of 24 h, the low temporal and spatial resolution of the pressure data itself, as well as uncertainties in Green's function and in the ocean response model (McCarthy and Petit 2004, p. 85). The APL corrections resulting from the geophysical model can be used to adjust site coordinates, to correct original observations (Tregoning and van Dam 2005) and to estimate regression coefficients by fitting local pressure variations (van Dam et al.

1994; Kaniuth and Vetter 2006). The current IERS Conventions 2010 suggest the S_1–S_2 APL tidal model (RP03) derived from the ECMWF operational global surface pressure fields with a spatial resolution of 1.125°. The diurnal (S_1) and semi-diurnal (S_2) atmospheric tides exhibit amplitudes of up to 1.5 mm in the equatorial regions. Assuming that the oceans respond to the APL as the solid Earth, the three-dimensional surface displacements can be determined using the elastic Green's functions. Gridded values of the predicted surface displacements from the RP03 model are available online[4]. In fact, corrections for the vertical displacement are usually sufficient (Petit and Luzum 2010, p. 112).

Recent studies presented in Dach et al. (2010) showed the advantages of applying the APL corrections at the GPS observation level as well as their impacts on geodetic datum definition and precise orbit determination. According to Steigenberger et al. (2009), parts of the APL-induced deformation may be absorbed by the troposphere modelling when using the GPT together with the GMF. This can be prevented by applying the ECMWF-derived a priori ZDD and the VMF1 so that the complete APL effect remains in the site coordinate estimates. At the time of writing, APL displacements have not been considered in the IGS products. However, in order to improve the quality of GPS data analysis, the IGS AC are required to apply the APL corrections, for example, by means of the RP03 model.

Further loading displacements. Further loading effects due to changes in snow and ice cover, soil moisture and groundwater, as well as in ocean-bottom pressure, also contribute to site displacements. Nominally, they have a comparable or smaller magnitude than the APL. However, at seasonal time scales, hydrological loads may cause larger surface displacements than air pressure, reaching up to 30 mm in the vertical component (Blewitt et al. 2001; Schuh et al. 2004). Models for non-tidal motions associated with changing environmental loads are still under development. Thus, they are not included in the current IERS Conventions 2010 (Petit and Luzum 2010, p. 99). Since the unmodelled loading effects remain as signals in the geodetic time series results, they can be extracted in post-analysis studies, for example, based on long-term (several years) GPS coordinate time series and GRACE (Gravity Recovery And Climate Experiment) surface load estimates (Tregoning et al. 2009).

Relativistic Effects

Effects on the equation of motion. The major acceleration correction to the equation of motion, known as the Schwarzschild term, is due to the general relativistic curvature of space-time caused by the Earth's gravity field. In the case of GPS, it can reach up to $3 \cdot 10^{-10}$ ms^{-2} (Zhu and Groten 1988). The much smaller effects of the de Sitter precession ($2 \cdot 10^{-11}$ ms^{-2}) and the Lense-Thirring precession ($1 \cdot 10^{-12}$ ms^{-2}) can be neglected (Steigenberger 2009, p. 36). While the Schwarzschild term primarily results in a secular shift in the argument of perigee, the Lense-Thirring

[4] http://geophy.uni.lu/ggfc-atmosphere/tide-loading-calculator.html

and de Sitter effects cause precessions of the orbital plane. Within the context of orbit determination, the neglect of the Schwarzschild term may lead to an apparent reduction of the orbit radius by 4 mm for circular orbits at all heights (Petit and Luzum 2010, p. 156).

Shapiro (gravitational) time delay. The Shapiro time delay, in this case, describes the increased propagation time of GPS signals due to the space-time curvature induced by the Earth's gravity field. The propagation correction to obtain the Euclidean distance depends on the geometry between the station, the satellite and the geocentre, amounting to a maximum of about 19 mm. Note that this maximum only applies to absolute point positioning (Zhu and Groten 1988; Hofmann-Wellenhof et al. 2008, p. 145).

Effects on satellite clocks. By convention, the relativistic effects on satellite clocks are subdivided into a constant and a periodic component. The constant part is attributed to both general and specific relativity caused by the gravitational potential differences and the mean satellite velocity, respectively. This component can be compensated by shifting the nominal frequency ($f_0 = 10.23$ MHz) of all GPS satellite frequency standards by a constant clock rate of $\Delta f/f_0 = -4.4647 \cdot 10^{-10}$ (ICD-GPS-200C 1993, p. 11), which indicates that the standard clock in orbit will run faster by 38.575 μs/day. More specifically, the general relativistic time gain due to the satellite's altitude is about 45.6 μs/day, while the special relativistic time loss because of the satellite's orbital speed is about 7.2 μs/day (Mungan 2006). Based on empirical analyses of the IGS final combined clock products, Kouba (2002a) found that the differences in the constant part are quite insignificant from satellite to satellite (i.e., about 0.01 μs/day). Taking the different mean orbit altitudes of the GPS satellites into consideration, the actual relativistic frequency offset for an individual satellite can differ from the constant clock shift by up to 10^{-13} (Petit and Luzman 2010, p. 154).

The periodic part is primarily due to the eccentricity of the satellite's orbit. The amplitude of the periodic correction is proportional to the orbit eccentricity e_o, amounting to about $2.29 \cdot e_o$ μs. For GPS orbits, e_o can reach up to 0.02, leading to a maximum clock correction of 46 ns (Kouba 2002a; Petit and Luzum 2010, p. 154). This conventional periodic correction given in ICD-GPS-200C (1993, p. 88) has been applied by the IGS for its official GPS and GLONASS clock products. However, it can introduce small clock rate errors of up to about 0.2 ns/day, as well as periodic errors with amplitudes of about 0.1 and 0.2 ns, and periods of about 6 h and 14 days, respectively. These small relativistic error effects are caused by the gravity field oblateness term J_2 and will become more significant for the future GPS and Galileo satellites which are equipped with better frequency standards. While the small clock rates and the 14 day periodic errors are completely absorbed into the daily clock rates, the 6 h periodic effects necessitate frequent clock estimation and distribution (e.g., hourly; Kouba 2004).

Effects on receiver clocks. The Sagnac effect describes a relativistic effect on the receiver clock induced by the Earth's rotation while the GPS signal propagates from the satellite to the receiver. It can lead to a relative frequency shift of $\Delta f/f_0 = 10^{-12}$, corresponding to a clock error of 10 ns or 3 m after 3 h (Hofmann-Wellenhof et al. 2008, p. 147). The Sagnac effect is generally corrected by the receiver software, and a detailed description of the correction model is provided by Marmet (2000). For more information about relativity in GPS, see, for example, Ashby (2002), Kouba (2002a, 2004) and Petit and Luzum (2010, Chap. 10).

3.2.4 Stochastic Model

In addition to the functional model defining the mathematical relationship between GPS measurements and the unknown parameters, the stochastic model describing the observation's statistical properties is also needed for a least-squares (LS) evaluation. The stochastic model is generally expressed by a variance-covariance matrix (VCM) that characterises the observations' precision and correlations by the main and off-diagonal elements, respectively (Tiberius et al. 1999). To obtain the best linear unbiased parameter estimates, the inverse of the cofactor matrix $\boldsymbol{Q}_{ll}$ should be used as the weight matrix $\boldsymbol{W}$ in the LS algorithm (see Sect. 2.1.3). As presented in Table 2.2, the stochastic model affects not only the estimates, but also the accuracy measures of the unknown parameters such as phase ambiguities (Teunissen et al. 1998; Teunissen 2000; Wang et al. 2002; Luo et al. 2008a,d), site coordinates (Howind et al. 1999; Jin et al. 2005; Schön and Brunner 2008b) and troposphere parameters (Jin and Park 2005; Luo et al. 2008a,c,d). A realistic accuracy assessment plays a key role in quality control and integrity monitoring (Teunissen 1998; Kim and Langley 2001; Wieser and Brunner 2002).

In contrast to the functional model, which has been intensively investigated by accounting for a majority of the error sources and effects discussed in Sect. 3.2.3, the commonly used stochastic model (VCM) still exhibits deficiencies arising from unrealistic observation weighting (variances) and the neglect of physical correlations between GPS measurements (covariances). The physical correlations can be subdivided into temporal, spatial and cross correlations that describe observational dependencies over time, in space and between frequencies, respectively. In order to achieve a better understanding of each constituent of the stochastic model, Fig. 3.2 displays schematically the structure of a fully populated VCM ($\boldsymbol{C}_{\boldsymbol{Z}}$) of the original undifferenced GPS phase observations from one station (R) to four satellites (j, k, l, r) at two epochs (t_1, t_2).

The main diagonal elements of the VCM characterise the observation quality and are different from each other with respect to satellite, frequency and epoch, i.e.,

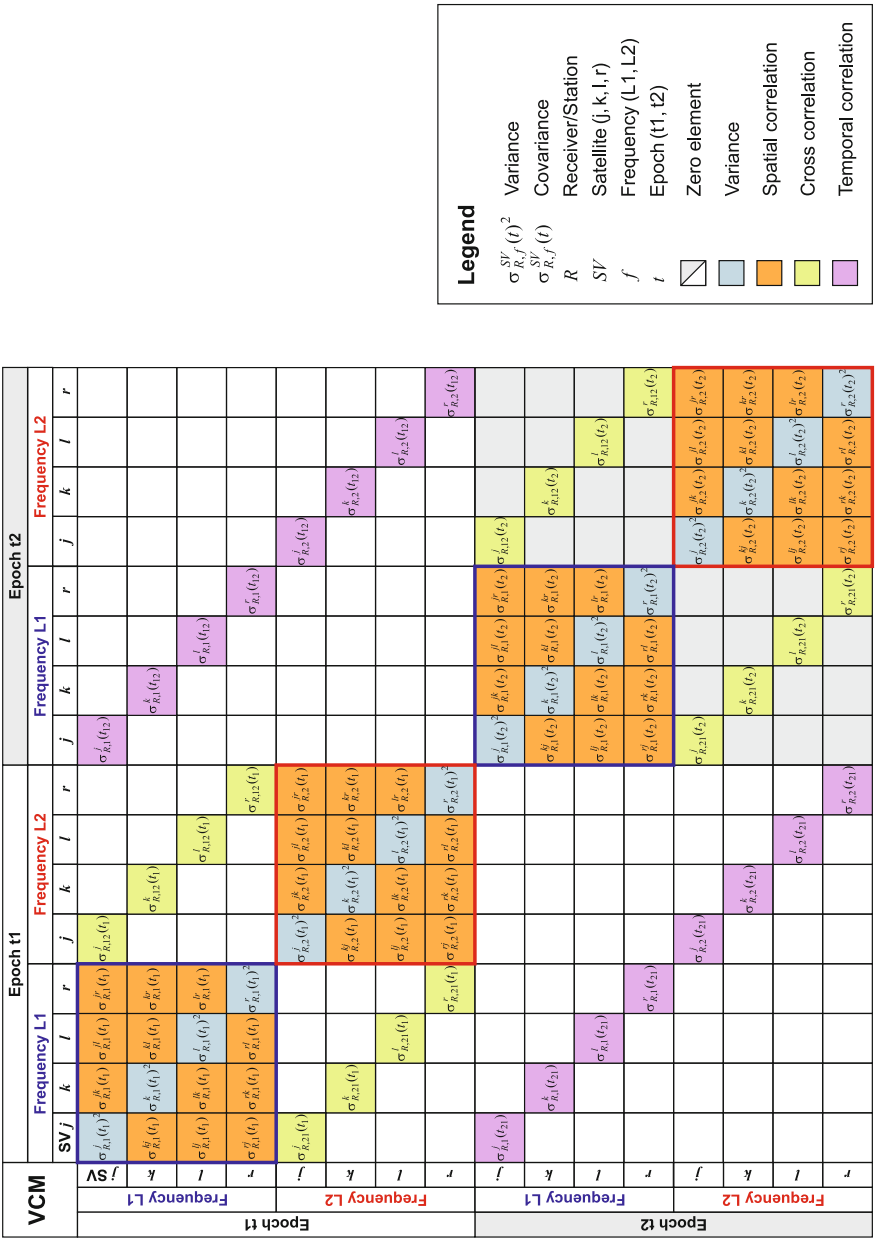

Fig. 3.2 Schematical presentation of a fully populated variance-covariance matrix (VCM) $\boldsymbol{C_Z}$ of the original undifferenced phase observations in PPP (SV: space vehicle)

$$\left[\sigma^{j}_{R,1}(t_1)\right]^2 \neq \left[\sigma^{k}_{R,1}(t_1)\right]^2, \quad \left[\sigma^{j}_{R,1}(t_1)\right]^2 \neq \left[\sigma^{j}_{R,2}(t_1)\right]^2,$$
$$\left[\sigma^{j}_{R,1}(t_1)\right]^2 \neq \left[\sigma^{j}_{R,1}(t_2)\right]^2. \tag{3.26}$$

The off-diagonal elements represent the different types of physical correlations, where the so-called inter-physical correlations, including more than one correlating component [e.g., $\sigma^{jk}_{R,12}(t_1)$, $\sigma^{jk}_{R,1}(t_{12})$, $\sigma^{j}_{R,12}(t_{12})$], are assumed to be absent. Using a simplified VCM, for example, only containing the diagonal elements of variances, will result in biased parameter estimates and over-optimistic formal accuracy measures (El-Rabbany 1994, p. 21; Howind 2005, p. 30). In the following text, the main properties of the stochastic components are described.

Variance

The variance of an individual GPS observation σ^2 can be obtained based on the a priori variance factor σ_0^2 and the associated weight w using $\sigma^2 = \sigma_0^2/w$ (Hofmann-Wellenhof et al. 2008, p. 239). The necessity of appropriate observation weighting arises from the fact that the GPS measurements from different satellites at different epochs cannot have the same precision (e.g., due to different atmospheric effects). A precise observation should have a higher weight (or lower variance) and contribute more to parameter estimation than an imprecise one. In statistical inferences and quality control processes, improper weights may cause outliers to remain undetected and truly high-quality observations to be rejected, leading to a considerable loss of accuracy in spite of largely redundant observations. However, in the practice of GPS data analysis, a realistic observation weighting turns out to be a difficult task due to various factors such as tracking loop characteristics, receiver and antenna hardware properties, signal strength, receiver dynamics, multipath and atmospheric effects, and so forth (Wieser 2007).

The simplest weighting scheme assigns an identical weight of $w = 1$ to all observations of the same type recorded by the same receiver. Under the assumption of uncorrelated GPS measurements, the VCM represents a scaled identity matrix. Due to the unrealistic assumptions of uncorrelatedness and homoscedasticity (i.e., homogeneity of variance), this simplified stochastic model is inadequate for high-precision GPS applications, particularly when including low-elevation observations (Luo et al. 2007c; Wieser 2007; Satirapod and Luansang 2008). The commonly applied variance model for GPS phase observations, other than a scaled identity matrix, uses the satellite elevation angle as an indicator for observation quality. The basic idea behind the elevation-dependent weighting concept is that observations at lower elevation angles suffer more strongly from atmospheric and multipath effects, hence are more noisy than those at higher elevation angles. Table 3.6 summarises some commonly used elevation-dependent variance models and the associated weight functions derived with respect to the geometrically optimum observation in the zenith direction. By

Table 3.6 Commonly used variance functions depending on the satellite elevation angle e

Notation	Variance function	σ_0^2 $(e = 90°)$	Weight function
CSC1	$\sigma^2 = \sigma_0^2/[2\sin(e)]$ if $e < 30°$ $\sigma^2 = \sigma_0^2$ if $e \geq 30°$	σ_0^2	$w = \dfrac{\sigma_0^2}{\sigma^2}$
CSC2	$\sigma^2 = a^2 + b^2/\sin^2(e)$	$a^2 + b^2$	
CSC3	$\sigma^2 = [c + d/\sin(e)]^2$	$(c + d)^2$	
EXP	$\sigma^2 = \left[m + n \cdot \exp(-e/e_0)\right]^2$	$\left[m + n \cdot \exp(-90°/e_0)\right]^2$	

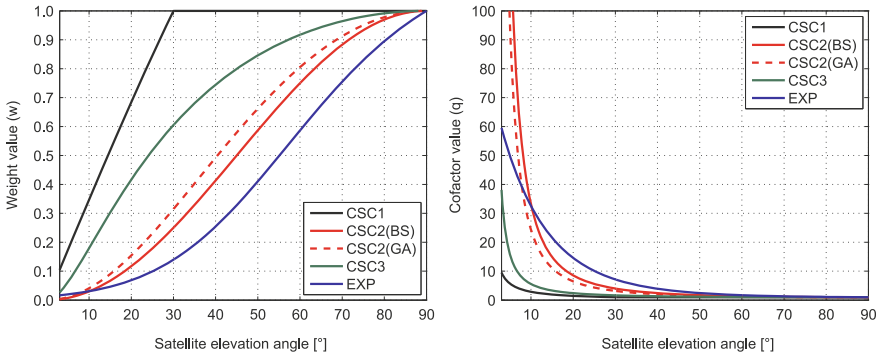

(a) Weight value w **(b)** Cofactor value $q = 1/w$

Fig. 3.3 Comparison of the commonly used elevation-dependent weight and cofactor functions presented in Table 3.6 (CSC2(BS): $a = 0$ mm, $b = 1$ mm, Dach et al. 2007, p. 144; CSC2(GA): $a = 4.3$ mm, $b = 7$ mm, King and Bock 2002, Chap. 5, pp. 9, 12; CSC3: $c = 5$ cm, $d = 2$ cm, Ray and Griffiths 2008; EXP: $m = 0.3$ cm, $n = 2.6$ cm, $e_0 = 20°$, Han 1997)

specifying representative model parameters, these weight functions and the corresponding cofactor values ($q = 1/w$) are compared in Fig. 3.3.

Comparing the weight and cofactor values shown in Fig. 3.3, particularly for low satellite elevation angles between 3 and 10°, these elevation-dependent weight functions can be categorised into three groups: (1) CSC2 strongly downweighting low-elevation observations, (2) CSC1 and CSC3 producing significantly higher weights at low elevation angles and (3) EXP appearing to be a compromise between (1) and (2). For elevation angles larger than about 55°, the maximum difference in the cofactor values is less than one. The variance function CSC2(BS) has been implemented in the Bernese GPS Software 5.0 (Dach et al. 2007, p. 144), while the variance model CSC2(GA) is available in the GAMIT GPS data analysis package (King and Bock 2002, Chap. 5, p. 9). The CSC1 and CSC3 are employed by the IGS analysis centres (AC) GFZ (Geo-ForschungsZentrum, Potsdam, Germany) and NGS (National Geodetic Survey, NOAA, USA), respectively. A detailed overview of the observation weighting schemes used by the IGS AC is provided by Ray and Griffiths (2008). In comparison to the widely used cosecant (CSC) construction, the exponential variance function EXP proposed by Euler and Goad (1991) has the advantage of non-

singularity in $e = 0°$. The model parameters m, n and e_0 (see Table 3.6) can be determined depending on the receiver and observation types.

The elevation-dependent variance models assume a strong correlation between the satellite elevation angle and GPS signal quality. They become inefficient for observations which are strongly affected by multipath effects, signal diffraction and receiver characteristics. For measurements collected under non-ideal observational conditions, direct signal quality measures such as signal-to-noise ratio (SNR; see Sect. 5.1) are more appropriate to assess the quality of GPS observations. In addition, since SNR values are generally available on both L1 and L2, the SNR-based variance models account for the frequency-related differences in observation quality. Langley (1997) showed the large potential of SNR as a key parameter in analysing GPS receiver performance and provided a SNR-based variance model for phase observations. In Sect. 5.2, this variance model will be discussed in more detail.

Instead of properly specifying σ_0 and w, the variance of an individual GPS observation can be determined using variance component estimation (VCE), for example, by means of the MINQUE (minimum norm quadratic unbiased estimation) procedure (Rao 1970, 1971). While the elevation-dependent and SNR-based variance models use the observed information before a LS adjustment is performed, the VCE is carried out based on the residuals obtained from a LS evaluation. The basic assumption is that the LS residuals represent the same statistical properties as the true errors if the observation period is long enough to remove all systematic effects. Comprehensive details of employing the VCE technique to estimate variance-covariance components of GPS observations can be found in Wang et al. (1998), Satirapod et al. (2002), Tiberius and Kenselaar (2003), Amiri-Simkooei (2007), Li et al. (2008, 2011) and Amiri-Simkooei et al. (2009). Moreover, Bischoff et al. (2005, 2006) provided test methods to statistically verify the hypothesis of heterogeneous variances, and estimation procedures to determine the values of variances. For GPS PPP, Satirapod and Luansang (2008) compared the MINQUE method with a scaled identity matrix and an elevation-dependent variance model of the cosecant construction. Thereby, the stochastic model estimated using the MINQUE method produced the most accurate coordinate estimates of both the horizontal and vertical components.

Covariance

The covariances are the off-diagonal elements of the VCM and represent the different kinds of physical correlations between GPS observations, such as the spatial correlation between different channels [e.g., $\rho^{jk}_{R,1}(t_1)$], the cross correlation between the L1 and L2 carriers [e.g., $\rho^{j}_{R,12}(t_1)$], and the temporal correlation between different epochs [e.g., $\rho^{j}_{R,1}(t_{12})$]. On the basis of the covariances, the corresponding correlation coefficients quantifying the observational dependencies in space, between frequencies, and over time can be expressed as

$$\rho_{R,1}^{jk}(t_1) = \frac{\sigma_{R,1}^{jk}(t_1)}{\sigma_{R,1}^{j}(t_1) \cdot \sigma_{R,1}^{k}(t_1)}, \quad \rho_{R,12}^{j}(t_1) = \frac{\sigma_{R,12}^{j}(t_1)}{\sigma_{R,1}^{j}(t_1) \cdot \sigma_{R,2}^{j}(t_1)},$$
$$\rho_{R,1}^{j}(t_{12}) = \frac{\sigma_{R,1}^{j}(t_{12})}{\sigma_{R,1}^{j}(t_1) \cdot \sigma_{R,1}^{j}(t_2)}. \tag{3.27}$$

Usually, the physical correlations are not considered in the stochastic model of GPS observations. The spatial correlation between the observations from one site to different satellites or from different sites to one satellite within one epoch is due to the similar observational conditions for these measurements. In fact, this kind of correlation makes the differencing technique applied in relative positioning effective in mitigating error effects (see Sect. 3.3.3). Intuitively, observations being spatially close to each other are more strongly correlated than those with a large spatial distance. Applying the VCE method to residuals from a zero-baseline, Tiberius and Kenselaar (2003) detected insignificant spatial correlation coefficients of the order of −0.1–0.1, which cannot be directly transferred into PPP.

Analysing time series of the LS residuals on L1 and L2, Tiberius et al. (1999) found considerable positive correlation between the L1 and L2 phase observations, particularly for the C1/X2 cross-correlation receivers. The detected cross-correlation coefficients range between 0.3 and 0.7, depending on the receiver type. The correlation between code and phase observations seems negligible (see also Bonna 2000). Using the VCE technique, these results were verified by Tiberius and Kenselaar (2003). Recent LS-VCE studies such as Amiri-Simkooei et al. (2009) showed significant positive correlations of up to 0.8 between the L1 and L2 phase observations.

Since the residual systematic errors change slowly over time, temporal correlation may exist between the observations from one site to the same satellite at different epochs. The temporal correlation behaviour of GPS observations depends not only on the satellite geometry, but also on the prevailing atmospheric conditions (e.g., wind speed and direction; Schön and Brunner 2008a), the site-specific effects (e.g., multipath impact; Amiri-Simkooei and Tiberius 2007; Nahavandchi and Joodaki 2010) and the receiver characteristics (e.g., signal smoothing and filtering; Tiberius et al. 1999; Amiri-Simkooei and Tiberius 2007). The larger the temporal separation distance is, the weaker the temporal correlation will be. Applying atmospheric turbulence theory to GPS carrier-phase data, Schön and Brunner (2008b) determined temporal correlation lengths of about 300–600 s for GPS double-difference observations. Smaller correlation lengths can be expected in the case of PPP, since the double differencing procedure may increase the correlation time of GPS phase observations (Nahavandchi and Joodaki 2010).

Variance-Covariance Propagation

The weight matrix $\boldsymbol{W_Z}$ derived from the VCM $\boldsymbol{C_Z}$ of the original phase observations $\boldsymbol{\Phi_Z}$, as shown in Fig. 3.2, cannot be directly substituted into Eq. (3.21) for $\boldsymbol{W_{Z3}}$ of the LC3 measurements $\boldsymbol{\Phi_{Z3}}$. Relying upon the linear relationship between $\boldsymbol{\Phi_Z}$ and

$\boldsymbol{\Phi}_{\boldsymbol{Z3}}$ formulated by the matrix $\boldsymbol{D}_{\boldsymbol{Z}}$, the VCM of $\boldsymbol{\Phi}_{\boldsymbol{Z3}}$, which is denoted as $\boldsymbol{C}_{\boldsymbol{Z3}}$, can be obtained by applying the variance-covariance propagation law to $\boldsymbol{C}_{\boldsymbol{Z}}$ as

$$\boldsymbol{\Phi}_{\boldsymbol{Z3}} = \boldsymbol{D}_{\boldsymbol{Z}} \cdot \boldsymbol{\Phi}_{\boldsymbol{Z}}, \quad \boldsymbol{C}_{\boldsymbol{Z3}} = \boldsymbol{D}_{\boldsymbol{Z}} \cdot \boldsymbol{C}_{\boldsymbol{Z}} \cdot \boldsymbol{D}_{\boldsymbol{Z}}^{T}. \tag{3.28}$$

In fact, the matrix $\boldsymbol{D}_{\boldsymbol{Z}}$ expresses the ionosphere-free linear combination LC3 in a matrix form and contains predominantly zero elements and the real-valued LC3 coefficients $k_{1,3}$ and $k_{2,3}$ [see Eq. (3.3) and Table 3.3]. According to the variance-covariance structure shown in Fig. 3.2, Fig. 3.4 displays the construction of $\boldsymbol{\Phi}_{\boldsymbol{Z}}$, $\boldsymbol{D}_{\boldsymbol{Z}}$ and $\boldsymbol{\Phi}_{\boldsymbol{Z3}}$. The matrix $\boldsymbol{C}_{\boldsymbol{Z3}}$ computed using Eq. (3.28) represents a fully populated VCM for the LC3 observations. The corresponding weight matrix $\boldsymbol{W}_{\boldsymbol{Z3}}$ can be calculated as $\boldsymbol{W}_{\boldsymbol{Z3}} = (\boldsymbol{C}_{\boldsymbol{Z3}}/\sigma_3^2)^{-1}$, where σ_3 is given by Eq. (3.7). Then, $\boldsymbol{W}_{\boldsymbol{Z3}}$ is used to estimate the unknown parameters in a LS adjustment, along with the LC3 observation vector $\boldsymbol{\Phi}_{\boldsymbol{Z3}}$ and the design matrix $\boldsymbol{A}$ [see Eq. (3.19)].

Benefiting from the continuously improved orbit and clock products, PPP has become a powerful technique with a promising future during the course of GNSS evolution. To exploit its full accuracy potential, numerous studies have been carried out aiming at ambiguity resolution, the integration of PPP with RTK and INS (inertial navigation system), and the incorporation of precise atmospheric models (Bisnath and Gao 2009). In contrast, little attention has been paid to the stochastic model which undoubtedly plays a key role in outlier detection and integrity monitoring. Focusing on the temporal correlation of GPS observation noise, Chaps. 7 and 8 will extend the PPP stochastic model in a mathematically rigorous manner.

3.3 Relative Positioning

Relative positioning employs at least two receivers simultaneously tracking the same satellites to determine the coordinates of an unknown point relative to a reference site with precisely known coordinates. Benefiting from the differencing technique, relative positioning generally provides a higher accuracy than autonomous positioning. Since the principle and the functional model of relative positioning are well documented in GPS literature (Hofmann-Wellenhof et al. 2008, Sect. 6.3), this section gives a more detailed discussion of the error effects and the stochastic model with respect to its structure, derivation and differences from that of PPP.

3.3.1 Introduction

For relative positioning, a minimum of four visible satellites is required at both the reference site and the remote site with unknown position. Assuming that GPS observations are sufficiently simultaneous (Wanninger 2000, p. 11), single-, double-, and triple-differences can be formed between receivers, satellites, and epochs. The

Vector and matrix	Epoch t1						Epoch t2					
	Frequency L1			Frequency L2			Frequency L1			Frequency L2		
	j	k	l	j	k	l	r	j	k	l	r	j	k	l	r
$\boldsymbol{\Phi}_{\boldsymbol{Z}}^{T}$	$\overset{j}{R,1}(t_1)$	$\overset{k}{R,1}(t_1)$	$\overset{l}{R,1}(t_1)$	$\overset{j}{R,2}(t_1)$	$\overset{k}{R,2}(t_1)$	$\overset{l}{R,2}(t_1)$	$\overset{r}{R,2}(t_1)$	$\overset{j}{R,1}(t_2)$	$\overset{k}{R,1}(t_2)$	$\overset{l}{R,1}(t_2)$	$\overset{r}{R,1}(t_2)$	$\overset{j}{R,2}(t_2)$	$\overset{k}{R,2}(t_2)$	$\overset{l}{R,2}(t_2)$	$\overset{r}{R,2}(t_2)$
$\boldsymbol{D}_{\boldsymbol{Z}}$	$k_{1,3}$			$k_{2,3}$				$k_{1,3}$				$k_{2,3}$			
		$k_{1,3}$			$k_{2,3}$				$k_{1,3}$				$k_{2,3}$		
			$k_{1,3}$			$k_{2,3}$				$k_{1,3}$				$k_{2,3}$	
				$k_{1,3}$			$k_{2,3}$				$k_{1,3}$				$k_{2,3}$

LC3 observation vector	$\boldsymbol{\Phi}_{\boldsymbol{Z3}}$	
Epoch t1	j	$\Phi^{j}_{R,3}(t_1)$
	k	$\Phi^{k}_{R,3}(t_1)$
	l	$\Phi^{l}_{R,3}(t_1)$
	r	$\Phi^{r}_{R,3}(t_1)$
Epoch t2	j	$\Phi^{j}_{R,3}(t_2)$
	k	$\Phi^{k}_{R,3}(t_2)$
	l	$\Phi^{l}_{R,3}(t_2)$
	r	$\Phi^{r}_{R,3}(t_2)$

Fig. 3.4 Construction of $\boldsymbol{\Phi}_{\boldsymbol{Z}}$, $\boldsymbol{D}_{\boldsymbol{Z}}$ and $\boldsymbol{\Phi}_{\boldsymbol{Z3}}$ corresponding to the VCM illustrated in Fig. 3.2

terminus single-difference used in this thesis involves two receivers and one satellite. This kind of single-difference eliminates the satellite clock bias and hardware delay. In addition, atmospheric and orbit errors are reduced, particularly for short baselines. Nevertheless, the ambiguities of single-differences are still non-integer values due to the generally unequal receiver hardware delays. Double-differences are obtained by subtracting two single-differences referring to the same baseline. The elimination of the receiver clock biases is the main reason why double-differences are preferably used. Since both the satellite and receiver hardware delays are cancelled, the double-differenced phase ambiguities have the integer property. Triple-differences, resulting from differencing double-differences between two epochs, can be used to eliminate the time-invariant ambiguities, provided that the receivers did not loose lock within this time interval. The triple-difference solution serves as an important reference for cycle slip detection. Tropospheric effects, which usually do not change rapidly with time, are considerably reduced on the triple-difference level. However, this is not the case for ionospheric effects, which may show very rapid temporal variations, particularly in the high northern and southern latitudes (Dach et al. 2007, pp. 39, 116). Mathematical formulations for the differenced phase equations can be found in Hofmann-Wellenhof et al. (2008, Sect. 6.3.2).

Relative positioning can be performed in both static and kinematic modes, where the static relative positioning with phase measurements is currently the most accurate satellite-based positioning technique. Depending on the baseline length, the expected accuracy using geodetic-type receivers is normally 5 mm + 0.5 ppm for the horizontal components and 5 mm + 1 ppm for the vertical component, where ppm stands for parts per million. For short baselines of up to 20 km, ambiguity resolution is a key issue to ensure high-performance positioning. In this case, it is recommended to resolve L1 and L2 ambiguities directly (Dach et al. 2007, p. 182). For long baselines of up to several hundred kilometres or more, the ionosphere-free linear combination LC3 should be used along with the precise orbit product (El-Rabbany 2006, p. 73).

The kinematic relative positioning can be subdivided into the post-processed kinematic (PPK) and real time kinematic (RTK). The PPK method starts with a process known as receiver initialisation, where the initial integer ambiguities are first determined. Once the initialisation has been successfully accomplished, cm-level positioning accuracy can be achieved. The coordinates of the unknown points are obtained by post-processing the collected data. In an RTK operation, the initial ambiguities are resolved almost instantaneously using the so-called on-the-fly ambiguity resolution technique (Hofmann-Wellenhof et al. 2008, p. 217). Establishing data communication (e.g., VHF or UHF radio, cellular telephone), the base receiver measurements and coordinates are transmitted to the rover receiver whose built-in software processes the collected GPS data to obtain the rover's coordinates in real-time. The expected RTK positioning accuracy using geodetic-type receivers is 1 cm + 1 ppm horizontally and 2 cm + 1 ppm vertically. Under the same conditions, the positioning quality of the RTK method is slightly degraded in comparison to that of the PPK method. This is mainly due to the latency while preparing and transmitting the base data, which necessitates data extrapolation to mach the time tag of the rover receiver measurements (El-Rabbany 2006, pp. 76, 77).

To achieve rapid and reliable ambiguity resolution, the maximum baseline length in a single-base RTK positioning should not exceed 20 km. This limitation is due to the distance-dependent biases such as orbit errors and signal refraction in the atmosphere (see Sect. 3.3.3). However, these errors can be accurately modelled based on the observations from an array of GPS reference sites (Wanninger 2000, Chap. 4; Dai et al. 2001; Fotopoulos and Cannon 2001). This leads to an extension of the RTK positioning from a single base to a multi-base technique. Moreover, continuously operating reference station networks, for example, the German Satellite Positioning Service (SA*POS*®; Stronk and Wegener 2005), have been established to provide network RTK positioning services using the master-auxiliary concept (MAC; Brown et al. 2006), area correction parameters (FKP; Wübbena et al. 2001) and virtual reference stations (VRS; Wanninger 2002, 2003). More information about the principles, limitations and future challenges of network RTK is provided by Rizos (2003) and Wanninger (2004, 2006). Additional GPS relative positioning modes, such as rapid static and stop-and-go, can be found in El-Rabbany (2006, Chap. 5).

3.3.2 Functional Model

The functional model of relative positioning describes the mathematical relationship between double-differenced observations and the unknown parameters. Under the assumption of equal frequency $f = f^j = f^k$ for the satellite signals, which is true in the case of GPS by applying the code division multiple access (CDMA) technique, the simplified observation equation of phase double-differences relating to receivers A and B, satellites j and k, and frequency f is

$$\Phi^{jk}_{AB,f} = \rho^{jk}_{AB} + \lambda_f \cdot N^{jk}_{AB,f} + \epsilon^{jk}_{AB,f}, \tag{3.29}$$

where

ρ^{jk}_{AB} : double-difference of the geometrical ranges in m,
λ_f : wavelength of the carrier in m,
$N^{jk}_{AB,f}$: integer double-difference phase ambiguity in cycles,
$\epsilon^{jk}_{AB,f}$: random noise of the double-difference in m.

Such a simplification is valid for short baselines under ideal observational conditions (Wanninger 2000, p. 12). The term ρ^{jk}_{AB} contains the geometry and can be decomposed as

$$\rho^{jk}_{AB} = \rho^{k}_{AB} - \rho^{j}_{AB} = \rho^{k}_{B} - \rho^{k}_{A} - \rho^{j}_{B} + \rho^{j}_{A}. \tag{3.30}$$

Substituting Eq. (3.30) into (3.29), the simplified observation equation becomes

$$l_{AB,f}^{jk} = \rho_B^k - \rho_A^k - \rho_B^j + \rho_A^j + \lambda_f \cdot N_{AB,f}^{jk} + \epsilon_{AB,f}^{jk}. \tag{3.31}$$

In the case of relative positioning, the coordinates of the reference site (e.g., site A) are precisely known. Accordingly, the vector of unknown parameters consists of the coordinates of the rover site B and all double-difference ambiguities, i.e.,

$$\boldsymbol{x} = (X_B, Y_B, Z_B, N_{AB,f}^i)^T, \quad i = 1, \ldots, m_{sp}, \tag{3.32}$$

where m_{sp} denotes the number of the formed satellite pairs. Regarding all $l_{AB,f}^{jk}$ as a realisation of the vector of stochastic double-difference observables $\underline{\boldsymbol{l}}_{\boldsymbol{D}}$ and assuming zero-mean random observation noise, the functional model of static relative positioning reads

$$\mathrm{E}(\underline{\boldsymbol{l}}_{\boldsymbol{D}}) = \mathbf{F}(\boldsymbol{x}) = \rho_B^k - \rho_A^k - \rho_B^j + \rho_A^j + \lambda_f \cdot N_{AB,f}^{jk}. \tag{3.33}$$

The expansion of Eq. (3.33) into a Taylor series around the approximate position of the rover site B (X_{B0}, Y_{B0}, Z_{B0}) leads to the linearised model of observation equations in the matrix form $\boldsymbol{A} \cdot \boldsymbol{\Delta}\hat{\boldsymbol{x}} = \boldsymbol{\Delta l_D} + \boldsymbol{v}$. According to Hofmann-Wellenhof et al. (2008, p. 255), the design matrix $\boldsymbol{A}$ can be written as

$$\boldsymbol{A} = \left[\frac{\partial \mathbf{F}(\boldsymbol{x})}{\partial X_B}, \frac{\partial \mathbf{F}(\boldsymbol{x})}{\partial Y_B}, \frac{\partial \mathbf{F}(\boldsymbol{x})}{\partial Z_B}, \frac{\partial \mathbf{F}(\boldsymbol{x})}{N_{AB,f}^i} \right]_{i=1,\ldots,m_{sp}}^{\boldsymbol{x}=\boldsymbol{x}_0}, \tag{3.34}$$

where

$$\begin{aligned} &\frac{\partial \mathbf{F}(\boldsymbol{x})}{\partial X_B} = \frac{X_B - X^k}{\rho_B^k} - \frac{X_B - X^j}{\rho_B^j}, \quad \frac{\partial \mathbf{F}(\boldsymbol{x})}{\partial Y_B} = \frac{Y_B - Y^k}{\rho_B^k} - \frac{Y_B - Y^j}{\rho_B^j}, \\ &\frac{\partial \mathbf{F}(\boldsymbol{x})}{\partial Z_B} = \frac{Z_B - Z^k}{\rho_B^k} - \frac{Z_B - Z^j}{\rho_B^j}, \quad \frac{\partial \mathbf{F}(\boldsymbol{x})}{\partial N_{AB,f}^i} = 0 \text{ or } \lambda_f. \end{aligned} \tag{3.35}$$

The vector of reduced parameters $\boldsymbol{\Delta x}$ can be expressed as

$$\boldsymbol{\Delta x} = \boldsymbol{x} - \boldsymbol{x}_0 = (\Delta X_B, \Delta Y_B, \Delta Z_B, N_{AB,f}^i)^T, \quad i = 1, \ldots, m_{sp}. \tag{3.36}$$

From Eq. (3.33), the reduced observation for $l_{AB,f}^{jk}$ is

$$\Delta l_{AB,f}^{jk} = l_{AB,f}^{jk} - \mathbf{F}(\boldsymbol{x}_0) = l_{AB,f}^{jk} - \rho_{B0}^k + \rho_A^k + \rho_{B0}^j - \rho_A^j, \tag{3.37}$$

where the position of the reference site A is assumed to be known, and the approximate $N_{AB,f}^{jk}$ is equal to zero [cf. Eqs. (3.32) and (3.36)]. Once the design matrix $\boldsymbol{A}$, the vector of reduced double-difference observations $\boldsymbol{\Delta l_D}$ and the corresponding weight matrix $\boldsymbol{W_D}$ are available, the parameter estimate $\hat{\boldsymbol{x}} = \boldsymbol{x}_0 + \boldsymbol{\Delta}\hat{\boldsymbol{x}}$ and the asso-

ciated VCM $\boldsymbol{C}_{\hat{x}\hat{x}}$ can be obtained from a LS adjustment. Initially, the LS ambiguity estimates are float values. The fixing of the float ambiguities to their integer values, known as ambiguity resolution, fully exploits the high accuracy of phase observations and significantly improves the quality of parameter estimates. A detailed discussion of different ambiguity resolution algorithms is provided by Hofmann-Wellenhof et al. (2008, Sect. 7.2). For geodetic-type dual-frequency receivers, the optimum ambiguity resolution strategy primarily depends on the availability of high-quality code measurements on both carriers, as well as on the baseline and session length (Dach et al. 2007, p. 180).

3.3.3 Error Sources and Effects

For relative positioning using baselines, it seems reasonable to classify the error sources into distance-dependent and site-specific (distance-independent) effects. Depending on the baseline length, the spatially correlated errors, such as ionospheric and tropospheric refraction, will be reduced by differencing. In contrast, site-specific effects, for example, multipath, are individual for each station and may even be amplified when forming differences between observations (Schön 2010). Moreover, some effects can be completely neglected for cm-level relative positioning and for baselines less than 100 km, but they must be taken into account when processing long baselines (e.g., more than 500 km). This section briefly describes the effects of the error sources in the solution domain, with an emphasis on the distance-dependent factors. In Table 3.7, the relevant error effects limiting the relative positioning quality are listed.

Distance-Dependent Effects

Satellite orbit errors. For the influence of unmodelled satellite orbit errors on station coordinate estimates, a handy rule of thumb is available in Dach et al. (2007, p. 24). It provides the error in baseline length Δl as a function of the error in satellite orbit ΔO using

$$\Delta l \approx \frac{l}{d} \cdot \Delta O, \tag{3.38}$$

where l is the baseline length in km, and $d \approx 25{,}000$ km is the approximate distance between the satellite system and the survey area. Substituting the current accuracy specifications of the IGS products for GPS satellite orbits into Eq. (3.38), the resulting errors in baseline length are presented in Table 3.8. Obviously, for regional networks consisting of baselines shorter than 500 km, the expected errors in baseline length due to inaccurate satellite orbits are below 1 mm if the IGS ultra-rapid, rapid or final orbit products are used. Furthermore, satellite orbit errors may cause apparent network rotations (Beutler et al. 1989).

Table 3.7 Error effects limiting the relative positioning quality

Distance-dependent effects	Satellite orbit errors Ionospheric effects Tropospheric effects
Site-specific effects	Multipath effects Receiver antenna models
Other relevant effects	Satellite antenna models Satellite phase wind-up effect Site displacement effects Relativistic effects

Table 3.8 Approximate errors in baseline length (Δl) using different IGS products for GPS satellite orbits [see Eq. (3.38), unit: mm]

Baseline length [km]	Accuracy of the IGS orbit product [mm][a]			
	Broadcast	Ultra-rapid (P)[b]	Ultra-rapid (O)[b]	Rapid & Final
	1,000	50	30	25
10	0.4	0.0	0.0	0.0
100	4.0	0.2	0.1	0.1
500	20.0	1.0	0.6	0.5
1,000	40.0	2.0	1.2	1.0

[a] http://igscb.jpl.nasa.gov/components/prods.html
[b] P: predicted part, O: observed part

Ionospheric effects. An erroneous estimate of the ionospheric total electron content (TEC) affects single-frequency relative positioning primarily in the form of a scale error. For the maximum zenith angle $z_{\max} = 80°$ on a medium-latitude site, an underestimation of the TEC by 10 TECU (1 TECU = 10^{16} electrons/m^2) leads to a decrease in baseline length of 0.7 ppm (i.e., $l = 100$ km $\rightarrow \Delta l = 7$ cm; Santerre 1989, p. 108). The magnitude of this scale effect depends on the site location, solar activity and occurrence of sudden ionospheric disturbances. Using the ionosphere-free linear combination LC3, the ionospheric effects can be largely reduced. However, the employment of the LC3 has the disadvantages of complicated ambiguity resolution as well as increased multipath effects and observation noise. Therefore, for baselines of up to several kilometres, the LC3 is not recommended, and single-frequency relative positioning is even preferred for coordinate estimation (Wanninger 2000, p. 19). If dual-frequency observations are available, ionosphere models can be determined using the geometry-free linear combination LC4 on the zero- or double-difference level (see Table 3.3). Local and regional ionosphere models can be derived by applying two-dimensional Taylor series expansions, while continental and global

ionosphere maps can be generated with the help of spherical harmonic expansions (Dach et al. 2007, Chap. 12).

Tropospheric effects. According to Beutler et al. (1988), the troposphere biases in relative positioning can be subdivided into an absolute and a relative component. The absolute troposphere biases are caused by errors arising from tropospheric refraction which are common to both endpoints of a baseline. They mainly produce scale errors in the estimated baseline lengths. The relative troposphere biases are due to errors of tropospheric refraction at one endpoint of a baseline relative to the other. They primarily induce errors in the estimated station heights. Assuming uniformly distributed satellites above the observing sites, the impact of an absolute (ΔT_a^0) and a relative troposphere bias in the zenith direction (ΔT_r^0) can be calculated as

$$\frac{\Delta l}{l} = \frac{\Delta T_a^0}{R_E \cdot \cos(z_{\max})}, \quad \Delta h = \frac{\Delta T_r^0}{\cos(z_{\max})}, \tag{3.39}$$

where $R_E \approx 6371$ km is the Earth's radius, Δl is the error in baseline length, and Δh is the bias in station height (Dach et al. 2007, p. 240). For $z_{\max} = 80°$ or an elevation cut-off angle of 10°, Eq. (3.39) implies that an absolute troposphere bias of 7 cm causes a scale error of 0.06 ppm (i.e., $l = 100$ km $\rightarrow \Delta l = 6$ mm), whereas a relative troposphere bias of 1 mm already leads to an error of approximately 6 mm in the estimated station height. Note that relative troposphere errors are much more important for local and regional applications. Table 3.9 provides more numerical examples of the biases caused by the atmospheric effects in relative positioning.

In comparison to the satellite orbit errors, the atmospheric effects reach orders of magnitude above the noise level of GPS phase observations and play a dominant role in the error budget of relative positioning. Due to the fact that the tropospheric refraction originates from the lowest part of the Earth's atmosphere (99 % below 10 km) whereas the ionospheric shell height is about 400 km, the tropospheric effects are more site-specific and can be accounted for by estimating site-specific troposphere parameters and gradients in GPS data processing. However, using differenced observations in relative positioning, the resulting troposphere solutions may be biased by a constant offset, particularly for local and regional networks (i.e., $l < 500$ km; Kouba

Table 3.9 Examples of biases in baseline length (Δl) and station height (Δh) induced by atmospheric effects [see Eq. (3.39), unit: m]

Baseline length [km]	Ionosphere (Δl)	Troposphere (Δl)		Troposphere (Δh)	
	10 TECU (0.7 ppm)	$\Delta T_a^0 = 0.1$ m		$\Delta T_r^0 = 0.01$ m	
	$z_{\max} = 80°$	$z_{\max} = 80°$	$z_{\max} = 87°$	$z_{\max} = 80°$	$z_{\max} = 87°$
10	0.007	0.001	0.009	0.058	0.191
100	0.070	0.009	0.087	0.058	0.191
500	0.350	0.045	0.437	0.058	0.191
1,000	0.700	0.090	0.874	0.058	0.191

2009). To achieve the absolute level, an external tropospheric calibration is required, for example, by means of PPP or the IGS combined troposphere products (Byun and Bar-Sever 2009). Furthermore, the strong correlation between the zenith tropospheric delay and station height estimates can be considerably reduced by lowering the elevation cut-off angle. Appropriate handling of low-elevation observations requires advanced mapping functions (e.g., GMF, VMF1) on the one hand, and improved stochastic models (e.g., observation weighting) on the other.

Site-Specific Effects

Multipath effects. For precise relative positioning with short baselines, multipath represents the major systematic error source. Its impact on carrier-phases should generally not exceed about 1 cm under good satellite geometry over a reasonably long observation period. Nevertheless, a simple change of the receiver antenna height may increase the multipath effects and deteriorate the positioning results (Hofmann-Wellenhof et al. 2008, p. 155). In addition to the techniques employed in antenna and receiver design, different data-processing approaches have been proposed for multipath mitigation, such as wavelet algorithms (Xia and Liu 2001; Souza and Monico 2004; Satirapod and Rizos 2005; Zhong et al. 2008; Wu et al. 2009), SNR-based methods (Bilich 2006; Bilich and Larson 2007; Bilich et al. 2008; Rost and Wanninger 2009, 2010; Rost 2011), sidereal filtering (Zheng et al. 2005; Ragheb et al. 2007; Zhong et al. 2010; Lau 2012) and least mean square adaptive filters (Ge et al. 2000; Weinbach et al. 2009; Liu et al. 2011). Analysing the temporal characteristics of multipath errors by means of auto-covariance functions, Nahavandchi and Joodaki (2010) modelled multipath effects stochastically. Making use of the site environment information, for example, represented by a georeferenced 3D site digital model, Fan and Ding (2006) employed the electromagnetic modelling technique to determine GPS phase multipath signals and visualised their propagations in an urban 3D model. The variety of multipath mitigation methods indicates that a generally valid and applicable multipath model is still lacking, which is mainly attributed to its strong time- and location-dependent properties. For rapid static survey applications, longer observation periods are advisable in the presence of strong multipath interference.

Receiver antenna models. In short-baseline relative positioning using the same antenna type and orientation, phase centre corrections only insignificantly affect the estimated coordinates, because the satellite signals are received under the almost identical azimuth and elevation angles. Nonetheless, if different antenna types are used at either end of a baseline, receiver antenna models must be considered in accordance with the current IGS convention. For long-baseline solutions, even using the same antenna type, calibration effects will not cancel out due to the non-negligible differences in satellite geometry caused by the Earth's curvature. These effects increase if site-specific troposphere parameters are estimated (Menge et al. 1998). Analysing a baseline of about 100 km with elevation-dependent relative and absolute receiver antenna models, Mader (2001) reported height biases varying from several millime-

tres to several centimetres. Furthermore, the use of radome calibrations may influence the height component by more than 1 cm. Differences between individual antennas of the same antenna type may induce discontinuities in GPS coordinate time series. This can be handled either by individual absolute antenna calibrations (e.g., chamber and robot calibration; Steigenberger 2009, pp. 151, 153), or by relative calibrations with respect to an absolutely calibrated antenna.

Other Relevant Effects

Satellite antenna models. For cm-level relative positioning and baselines of less than 100 km, the influence of phase centre models of GPS satellite antennas can be safely neglected (Kouba 2009). However, the only use of absolute receiver antenna corrections was found to produce a global reference frame which differs from the results achieved with very long baseline interferometry (VLBI) and satellite laser ranging (SLR) by about 15 ppb (part per billion). This corresponds to a height variation of about 10 cm for all global sites (Rothacher 2001; Schmid and Rothacher 2003; Zhu et al. 2003). This scale problem was solved by additionally considering absolute satellite antenna PCO and PCV which have been successively estimated by fixing the absolute receiver antenna models and the terrestrial scale (Schmid et al. 2007). Note that all satellite antenna model parameters refer to the LC3, while an absolute receiver antenna calibration (e.g., robot-based) delivers phase centre corrections for L1 and L2. The use of absolute instead of relative receiver and satellite antenna models in GPS global solutions leads to decreased dependency of parameter estimates on the elevation cut-off angle (Schmid et al. 2005), improved orbit consistency, reduced biases in troposphere parameters, and vertical (horizontal) coordinate changes of up to about 2 cm (1 cm) (Schmid et al. 2007; Steigenberger 2009, Sect. 9.2). For the switch from ITRF05 to ITRF08, Dach et al. (2011) performed an update of the absolute IGS antenna phase centre model by a GLONASS extension of the reprocessed GPS-only products (Steigenberger 2009). The differences between the GPS- and GLONASS-specific receiver antenna PCV amount to 10 mm for the LC3. This update considerably affects site coordinates by up to 5 mm and most benefits GLONASS-only rapid static or kinematic solutions. Due to the antenna assembly and power supply, the satellite antenna PCV are actually azimuth-dependent (Czopek and Shollenberger 1993) and may cause changes in the horizontal components by up to about 1 cm (Steigenberger 2009, p. 149). However, this dependency is not considered in the current IGS phase centre model igs08 (Schmid 2010).

Satellite phase wind-up effect. In general, the satellite phase wind-up correction can be neglected for double-difference positioning on baselines or networks spanning up to a few hundred kilometres (Kouba 2009). However, for very long baselines (e.g., 4,000 km), this correction term has been shown to amount to 4 cm (Wu et al. 1993; Steigenberger 2009, p. 35). The receiver phase wind-up effect is fully absorbed

into station clock solutions or eliminated during the course of double differencing (Le and Tiberius 2006; Kouba 2009).

Site displacement effects. Since the site displacement effects discussed in Sect. 3.2.3 are nearly the same over large areas, they almost cancel out in relative positioning over short baselines (i.e., $l < 100$ km), and thus need not be considered. However, for baselines that are more than 500 km, the site displacement corrections must be computed and added to the regularised[5] ITRF coordinates to obtain the instantaneous position (Kouba 2009).

Relativistic effects. In terms of relativistic effects, the dynamic component (Schwarzschild term) and the Shapiro time delay which impact on satellite orbits and signal propagation, respectively, cannot be eliminated by differencing and cause errors of up to 0.001 ppm in positioning (i.e., 7 mm for a baseline of 7,000 km; Zhu and Groten 1988). Therefore, they should be considered in high-accuracy applications, for example, when generating satellite orbit products (Dach et al. 2007, p. 92). The influence on the satellite clock is completely cancelled out in the between-station differences and is harmless for relative positioning (Zhu and Groten 1988).

3.3.4 Stochastic Model

Since a double-difference is composed of four zero-differences, the stochastic model of relative positioning is more complex than that of PPP, particularly with regard to correlation type and structure. Instead of a description of the individual stochastic components, as is done for PPP, this section focuses on the mathematical correlation introduced during the course of double differencing, as well as on the variance-covariance structure and propagation. Finally, different approaches for completing and improving the stochastic model in relative positioning, especially with respect to modelling physical correlations, are briefly summarised.

Mathematical Correlation

If double-differenced observations are analysed, the so-called mathematical correlations between the differenced measurements must be taken into account, because the same original observation may be involved in different observation differences (Beutler et al. 1987). As shown by Santos et al. (1997), a proper modelling of mathematical correlations results in more accurate baseline lengths and more realistic formal errors of the estimated position differences. Nowadays, this type of correla-

[5] The purpose of introducing a regularised (conventional tide-free) position is to remove high-frequency time variations which are mainly caused by geophysical phenomena, in order to obtain a position with more regular time variations (Petit and Luzum 2010, p. 34).

tion has been successfully considered in both baseline and network solutions using high-end GPS analysis software, for example, the Bernese GPS Software 5.0 (Dach et al. 2007, p. 146). To gain a better understanding of how the mathematical correlation originates, let $\boldsymbol{\Phi_Z}$, $\boldsymbol{\Phi_S}$ and $\boldsymbol{\Phi_D}$ be the zero-, single- and double-difference phase observation vector relating to two receivers (A, B) and four satellites (j, k, l, r) observed at the same epoch:

$$\begin{aligned} \boldsymbol{\Phi_Z} &= (\Phi_A^j, \Phi_A^k, \Phi_A^l, \Phi_A^r, \Phi_B^j, \Phi_B^k, \Phi_B^l, \Phi_B^r)^T, \\ \boldsymbol{\Phi_S} &= (\Phi_{AB}^j, \Phi_{AB}^k, \Phi_{AB}^l, \Phi_{AB}^r)^T, \quad \boldsymbol{\Phi_D} = (\Phi_{AB}^{jk}, \Phi_{AB}^{jl}, \Phi_{AB}^{jr})^T, \end{aligned} \tag{3.40}$$

where the double- and single-differences are formed as

$$\Phi_{AB}^{jk} = \Phi_{AB}^k - \Phi_{AB}^j = (\Phi_B^k - \Phi_A^k) - (\Phi_B^j - \Phi_A^j). \tag{3.41}$$

The single- and double-differences can be computed from the matrix-vector relation as

$$\boldsymbol{\Phi_S} = \boldsymbol{D_Z} \cdot \boldsymbol{\Phi_Z}, \quad \boldsymbol{\Phi_D} = \boldsymbol{D_S} \cdot \boldsymbol{\Phi_S}, \tag{3.42}$$

where $\boldsymbol{D_Z}$ and $\boldsymbol{D_S}$ are

$$\boldsymbol{D_Z} = \begin{pmatrix} -1 & 0 & 0 & 0 & 1 & 0 & 0 & 0 \\ 0 & -1 & 0 & 0 & 0 & 1 & 0 & 0 \\ 0 & 0 & -1 & 0 & 0 & 0 & 1 & 0 \\ 0 & 0 & 0 & -1 & 0 & 0 & 0 & 1 \end{pmatrix}, \quad \boldsymbol{D_S} = \begin{pmatrix} -1 & 1 & 0 & 0 \\ -1 & 0 & 1 & 0 \\ -1 & 0 & 0 & 1 \end{pmatrix} \tag{3.43}$$

with j chosen as the reference satellite for double differencing. Assuming that the observation errors of $\boldsymbol{\Phi_Z}$ are mutually uncorrelated and exhibit a random behaviour following a normal distribution with expectation zero and variance σ_1^2, then the VCM of $\boldsymbol{\Phi_Z}$, $\boldsymbol{\Phi_S}$ and $\boldsymbol{\Phi_D}$ are

$$\boldsymbol{C_Z} = \sigma_1^2 \cdot \boldsymbol{I}, \quad \boldsymbol{C_S} = \boldsymbol{D_Z} \cdot \boldsymbol{C_Z} \cdot \boldsymbol{D_Z^T}, \quad \boldsymbol{C_D} = \boldsymbol{D_S} \cdot \boldsymbol{C_S} \cdot \boldsymbol{D_S^T}, \tag{3.44}$$

where $\boldsymbol{I}$ is a 8×8 identity matrix, and the matrices $\boldsymbol{C_S}$ and $\boldsymbol{C_D}$ are derived by means of the variance-covariance propagation law. Substituting Eq. (3.43) into (3.44) yields

$$\boldsymbol{C_S} = \sigma_1^2 \cdot \begin{pmatrix} 2 & 0 & 0 & 0 \\ 0 & 2 & 0 & 0 \\ 0 & 0 & 2 & 0 \\ 0 & 0 & 0 & 2 \end{pmatrix} = 2\sigma_1^2 \cdot \begin{pmatrix} 1 & 0 & 0 & 0 \\ 0 & 1 & 0 & 0 \\ 0 & 0 & 1 & 0 \\ 0 & 0 & 0 & 1 \end{pmatrix}, \tag{3.45}$$

$$\boldsymbol{C_D} = 2\sigma_1^2 \cdot \begin{pmatrix} 2 & 1 & 1 \\ 1 & 2 & 1 \\ 1 & 1 & 2 \end{pmatrix} = 4\sigma_1^2 \cdot \begin{pmatrix} 1 & 0.5 & 0.5 \\ 0.5 & 1 & 0.5 \\ 0.5 & 0.5 & 1 \end{pmatrix}. \tag{3.46}$$

The results clearly show that the single-differences are mathematically uncorrelated, while a mathematical correlation is present in the double-differences, with a correlation coefficient of 0.5. The derivations of mathematical correlations in double-differenced network solutions and in triple-differences are well documented in Hofmann-Wellenhof et al. (2008, pp. 181, 259).

Variance-Covariance Structure and Propagation

Equations (3.43) and (3.44) indicate that the mathematical correlation introduced by the double-differencing process is maintained when applying the variance-covariance propagation law to the VCM $\boldsymbol{C_Z}$ of the original undifferenced phase observation vector $\boldsymbol{\Phi_Z}$. Therefore, the structures of $\boldsymbol{C_Z}$, $\boldsymbol{D_Z}$ and $\boldsymbol{D_S}$ are essential for appropriately defining the stochastic model in relative positioning. Taking the temporal, spatial and cross correlations into account, Fig. 3.5 illustrates schematically the construction of a fully populated VCM of $\boldsymbol{\Phi_Z}$ relating to two stations (A, B), four satellites (j, k, l, r) and two epochs (t_1, t_2).

Under the assumption that the inter-physical correlations with more than one correlating component are absent (see Sect. 3.2.4), Fig. 3.5 primarily displays the covariance structure due to correlations with respect to satellite, station, frequency and epoch. While the spatial correlation in PPP exists only between observations from one receiver to different satellites, it is also present between observations from one satellite to different stations in relative positioning (see the black dashed line frames in Fig. 3.5). Intuitively, observations from short baselines are more strongly correlated in space than those from long baselines. The cross and temporal correlation structures shown in Fig. 3.5 represent an extension of Fig. 3.2 for two sites.

Regarding Eq. (3.42), it seems reasonable to accomplish the whole differencing process in a single step using

$$\boldsymbol{\Phi_D} = \boldsymbol{D_{SZ}} \cdot \boldsymbol{\Phi_Z}, \quad \boldsymbol{D_{SZ}} = \boldsymbol{D_S} \cdot \boldsymbol{D_Z}. \tag{3.47}$$

Applying Eq. (3.47) to the numerical example given in Eq. (3.43), the resulting matrix $\boldsymbol{D_{SZ}}$ is equal to

$$\boldsymbol{D_{SZ}} = \begin{pmatrix} 1 & -1 & 0 & 0 & -1 & 1 & 0 & 0 \\ 1 & 0 & -1 & 0 & -1 & 0 & 1 & 0 \\ 1 & 0 & 0 & -1 & -1 & 0 & 0 & 1 \end{pmatrix}, \tag{3.48}$$

where the number of columns (rows) of $\boldsymbol{D_{SZ}}$ corresponds to the number of zero-differences (double-differences). Instead of showing the structures of $\boldsymbol{D_Z}$ and $\boldsymbol{D_S}$ individually, Fig. 3.6 visualises the construction of $\boldsymbol{D_{SZ}}$ for deriving the LC3 double-difference observations $\boldsymbol{\Phi_{D3}}$ from $\boldsymbol{\Phi_Z}$ whose VCM is illustrated in Fig. 3.5. For the sake of simplicity, in this example, $\boldsymbol{D_{SZ}}$ has the same structure at different epochs t_1 and t_2. Depending on the satellite geometry and the choice of the reference satellite, the construction of $\boldsymbol{D_{SZ}}$ may differ from one epoch to another. Although

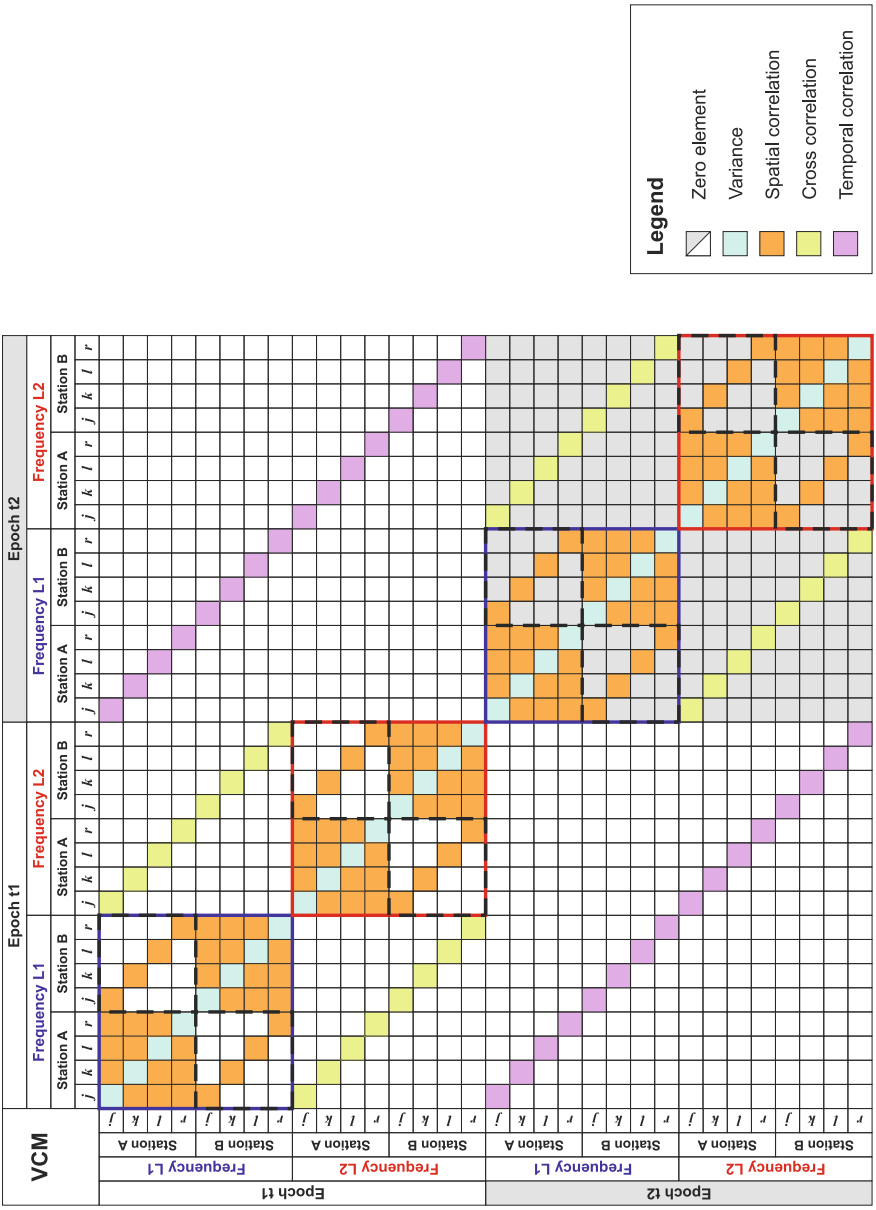

Fig. 3.5 Schematical presentation of a fully populated variance-covariance matrix (VCM) $\boldsymbol{C_Z}$ of the original undifferenced phase observations in relative positioning (cf. Fig. 3.2)

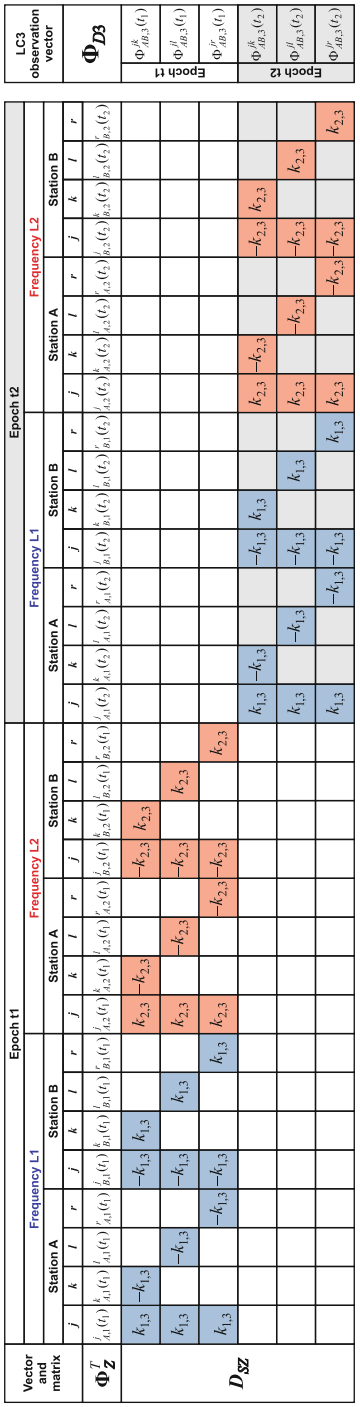

Fig. 3.6 Construction of $\boldsymbol{\Phi_Z}$, $\boldsymbol{D_{SZ}}$ and $\boldsymbol{\Phi_{D3}}$ corresponding to the VCM shown in Fig. 3.5

$\boldsymbol{D_{SZ}}$ is presented for the LC3 double-differences, it can be applied to other linear combinations using the corresponding coefficients given in Table 3.3. Based on the matrices $\boldsymbol{C_Z}$ and $\boldsymbol{D_{SZ}}$ depicted in Figs. 3.5 and 3.6, respectively, the VCM of $\boldsymbol{\Phi_{D3}}$ can be determined by applying the variance-covariance propagation law to Eq. (3.47) as

$$\boldsymbol{C_{D3}} = \boldsymbol{D_{SZ}} \cdot \boldsymbol{C_Z} \cdot \boldsymbol{D_{SZ}^T}. \tag{3.49}$$

The associated weight matrix $\boldsymbol{W_{D3}}$ can be computed as $\boldsymbol{W_{D3}} = \left(\boldsymbol{C_{D3}}/\sigma_3^2\right)^{-1}$, where σ_3 in relative positioning is equal to

$$\sigma_3 = 2\sigma_1 \cdot \sqrt{k_{1,3}^2 + k_{2,3}^2} \tag{3.50}$$

with the coefficients $k_{1,3}$ and $k_{2,3}$ provided in Table 3.3 (see also Howind 2005, p. 29). Using the fully-populated weight matrix $\boldsymbol{W_{D3}}$ together with the LC3 double-difference observation vector $\boldsymbol{\Phi_{D3}}$ and the design matrix $\boldsymbol{A}$ given in Eq. (3.34), a LS adjustment can be performed to estimate the unknown parameters such as site coordinates and phase ambiguities. Additional discussion of the VCM structure in relative positioning is available in Howind et al. (1999).

Improved Stochastic Models of GPS Observations

Up to now, different methods have been proposed to improve the stochastic model of GPS observations in relative positioning. Table 3.10 provides an overview of these methods with respect to variance and covariance modelling. While the elevation-dependent and SNR-based variance (or observation weighting) schemes are usually applied to the original undifferenced measurements, the VCE technique is often performed based on the residuals of differenced observations from zero and ultra-short baselines. Moreover, the VEC method has been successfully employed to study the covariance structure of GPS observations and receiver noise characteristics (Tiberius and Kenselaar 2003; Amiri-Simkooei and Tiberius 2007; Li et al. 2008, 2011; Amiri-Simkooei et al. 2009). Analysing time series of observation residuals, the temporal and spatial correlations haven been investigated by means of ACF, CCF, and ARMA processes (Bona 2000; Wang et al. 2002; Howind 2005, p. 57; Leandro and Santos 2007; Luo et al. 2012b). In addition to the mathematical approaches, the application of ATT enables a better understanding of the physical processes that correlate and decorrelate GPS phase observations (Schön and Brunner 2008a,b). It is worth mentioning that among all the listed techniques, the VCE method is the only one used to characterise all stochastic components.

In this thesis, an empirical SNR-based observation weighting model is developed and its effects on GPS relative positioning are investigated with respect to ambiguity resolution, troposphere parameter estimation and site coordinate determination. Furthermore, based on residual decomposition and ARMA modelling, a mathematically rigorous temporal correlation analysis is carried out and the

Table 3.10 Approaches to completing and improving the stochastic model of GPS observations

Stochastic component		Modelling methods						
		ELV[a]	SNR[b]	VCE[c]	ACF[d]	ARMA[e]	CCF[f]	ATT[g]
Variance (observation weighting)		X	X	X				X
Covariance	Spatial correlation			X		X	X	X
	Cross correlation			X		X	X	
	Temporal correlation			X	X	X		X

[a] ELV: satellite elevation angle
[b] SNR: signal-to-noise ratio
[c] VCE: variance component estimation
[d] ACF: autocorrelation function
[e] ARMA: autoregressive moving average
[f] CCF: cross-correlation function
[g] ATT: atmospheric turbulence theory

results are statistically verified, physically interpreted and experimentally used to extend the PPP stochastic model. Representative GPS data and freely available surface meteorological information are incorporated into three case studies which will be described in the next chapter, along with the applied GPS data processing strategies.

References

Alber, C., Ware, R., Rocken, C., & Braun, J. (2000). Obtaining single path phase delays from GPS double differences. *Geophysical Research Letters*, *27*(17), 2661–2664. doi:10.1029/2000GL011525.

Amiri-Simkooei, A. R. (2007). Least-squares variance component estimation: Theory and GPS applications. PhD thesis, Delft University of Technology, Publications on Geodesy, 64, Netherlands Geodetic Commission, Delft.

Amiri-Simkooei, A. R., & Tiberius, C. C. J. M. (2007). Assessing receiver noise using GPS short baseline time series. *GPS Solutions*, *11*(1), 21–35. doi:10.1007/s10291-006-0026-8.

Amiri-Simkooei, A. R., Teunissen, P. J. G., & Tiberius, C. C. J. M. (2009). Application of least-squares variance component estimation to GPS observables. *Journal of Surveying Engineering*, *135*(4), 149–160. doi:10.1061/(ASCE)0733-9453(2009)135:4(149).

Ashby, N. (2002). Relativity and the Global Positioning System. *Physics Today*, *55*(5), 41–47. doi:10.1063/1.1485583.

Ashjaee, J., & Lorenz, R. (1992). Precise GPS surveying after Y-code. In: *Proceedings of ION GPS 1992*. Albuquerque, NM, 16–18 Sep, pp. 657–659.

Ashkenazi, V. (2006). Geodesy and satellite navigation: A lighthearted look at a strange relationship. *Inside GNSS*, *1*(3), 44–49.

Awange, J. L. (2012). *Environmental monitoring using GNSS: Global Navigation Satellite Systems*. Berlin: Springer.

Baltink, H. K., van der Marel, H., & van der Hoeven, A. G. A. (2002). Integrated atmospheric water vapor estimates from a regional GPS network. *Journal of Geophysical Research*, *107*(D3), 4025. doi:10.1029/2000JD000094.

Bar-Sever, Y., Young, L., Stocklin, F., Heffernan, P., & Rush, J. (2004). NASA's global differential GPS system and the TDRSS augmentation service for satellites. In: *Proceedings of the 2nd ESA Workshop on Satellite Navigation User Equipment Technologies*, *NAVITEC 2004*, ESTEC, Noordwijk, The Netherlands, 8–10 Dec.

Bassiri, S., & Hajj, G. A. (1993). Higher-order ionospheric effects on the global positioning system observables and means of modeling them. *Manuscripta Geodetica*, *18*(6), 280–289.

Bender, M., & Raabe, A. (2007). Preconditions to ground-based GPS water vapour tomography. *Annales Geophysicae*, *25*(8), 1727–1734. doi:10.5194/angeo-25-1727-2007.

Bender, M., Dick, G., Wickert, J., Schmidt, T., Song, S., Gendt, G., et al. (2008). Validation of GPS slant delays using water vapour radiometers and weather models. *Meteorologische Zeitschrift*, *17*(6), 807–812. doi:10.1127/0941-2948/2008/0341.

Bender, M., Dick, G., Ge, M., Deng, Z., Wickert, J., Kahle, H.-G., et al. (2011a). Development of a GNSS water vapour tomography system using algebraic reconstruction techniques. *Advances in Space Research*, *47*(10), 1704–1720. doi:10.1016/j.asr.2010.05.034.

Bender, M., Stosius, R., Zus, F., Dick, G., Wickert, J., & Raabe, A. (2011b). GNSS water vapour tomography–Expected improvements by combining GPS, GLONASS and Galileo observations. *Advances in Space Research*, *47*(5), 886–897. doi:10.1016/j.asr.2010.09.011.

Beutler, G., Bauersima, I., Gurtner, W., & Rothacher, M. (1987). Correlations between simultaneous GPS double difference carrier phase observations in the multistation mode: Implementation considerations and first experience. *Manusripta Geodaetica*, *12*(1), 40–44.

Beutler, G., Baueršíma, I., Gurtner, W., Rothacher, M., Schildknecht, T., & Geiger, A. (1988). Atmospheric refraction and other important biases in GPS carrier phase observations. In: F. K. Brunner (Ed.), *Atmospheric effects on geodetic space measurements*, School of surveying monograph, No. 12, University of New South Wales, Kensington, pp. 15–43.

Beutler, G., Bauersima, I., Botton, S., Gurtner, W., Rothacher, M., & Schildknecht, T. (1989). Accuracy and biases in the geodetic application of the Global Positioning System. *Manuscripta Geodaetica*, *14*(1), 28–35.

Beutler, G., Brockmann, E., Gurtner, W., Hugentobler, U., Mervart, L., Rothacher, M., et al. (1994). Extended orbit modeling techniques at the CODE processing center of the International GPS Service for Geodynamics (IGS): Theory and initial results. *Manuscripta Geodetica*, *19*(6), 367–386.

Bevis, M., Businger, S., Herring, T. A., Rocken, C., Anthes, R. A., & Ware, R. H. (1992). GPS meteorology: Remote sensing of atmospheric water vapor using the Global Positioning System. *Journal of Geophysical Research*, *97*(D14), 15787–15801. doi:10.1029/92JD01517.

Bevis, M., Businger, S., Chiswell, S., Herring, T. A., Anthes, R. A., Rocken, C., et al. (1994). GPS meteorology: Mapping zenith wet delays onto precipitable water. *Journal of Applied Meteorology and Climatology*, *33*(3), 379–386. doi:10.1175/1520-0450(1994)033<0379:GMMZWD>2.0.CO;2.

Beyerle, G. (2009). Carrier phase wind-up in GPS reflectometry. *GPS Solutions*, *13*(3), 191–198. doi:10.1007/s10291-008-0112-1.

Bilich, A. L. (2006). Improving the precision and accuracy of geodetic GPS: Applications to multipath and seismology. PhD thesis, University of Colorado Boulder, Boulder.

Bilich, A., & Larson, K. M. (2007). Mapping the GPS multipath environment using the signal-to-noise ratio (SNR). *Radio Science*, *42*, RS6003. doi:10.1029/2007RS003652.

Bilich, A., Larson, K. M., & Axelrad, P. (2008). Modeling GPS phase multipath with SNR: Case study from the Salar de Uyuni, Boliva. *Journal of Geophysical Research*, *113*, B04401. doi:10.1029/2007JB005194.

Bischoff, W., Heck, B., Howind, J., & Teusch, A. (2005). A procedure for testing the assumption of homoscedasticity in least squares residuals: A case study of GPS carrier-phase observations. *Journal of Geodesy*, *78*(7–8), 397–404. doi:10.1007/s00190-004-0390-5.

Bischoff, W., Heck, B., Howind, J., & Teusch, A. (2006). A procedure for estimating the variance function of linear models and for checking the appropriateness of estimated variances: A case

study of GPS carrier-phase observations. *Journal of Geodesy*, *79*(12), 694–704. doi:10.1007/s00190-006-0024-1.

Bisnath, S. B., & Gao, Y. (2009). Precise point positioning: A powerful technique with a promising future. *GPS World*, *20*(4), 43–50.

Blewitt, G., Lavallée, D., Clarke, P., & Nurutdinov, K. (2001). A new global mode of the earth deformation: Seasonal cycle detected. *Science*, *294*(5550), 2342–2345. doi:10.1126/science.1065328.

Boehm, J., Niell, A., Tregoning, P., & Schuh, H. (2006a). Global Mapping Function (GMF): A new empirical mapping function based on numerical weather model data. *Geophysical Research Letters*, *33*, L07304. doi:10.1029/2005GL025546.

Boehm, J., Werl, B., & Schuh, H. (2006b). Troposphere mapping functions for GPS and very long baseline interferometry from European Centre for Medium-Range Weather Forecasts operational analysis data. *Journal of Geophysical Research*, *111*, B02406. doi:10.1029/2005JB003629.

Boehm, J., Heinkelmann, R., & Schuh, H. (2007). Short note: A global model of pressure and temperature for geodetic applications. *Journal of Geodesy*, *81*(10), 679–683. doi:10.1007/s00190-007-0135-3.

Bona, P. (2000). Precision, cross correlation, and time correlation of GPS phase and code observations. *GPS Solutions*, *4*(2), 3–13. doi:10.1007/PL00012839.

Brondeel, M., & Willems, T. (2003). Atmospheric pressure loading in GPS height estimates. *Advances in Space Research*, *31*(8), 1959–1964. doi:10.1016/S0273-1177(03)00157-1.

Brown, N., Geisler, I., & Troyer, L. (2006). RTK rover performance using the Master-Auxiliary concept. *Journal of Global Positioning Systems*, *5*(1–2), 135–144.

Bulletin C43-IERS (2012). UTC time step on the 1st of July 2012. Earth Orientation Center of the International Earth Rotation and Reference Systems Service (IERS), available online at ftp://hpiers.obspm.fr/iers/bul/bulc/bulletinc.43, accessed on 12 Mar, 2012.

Businger, S., Chiswell, S. R., Bevis, M., Duan, J., Anthes, R. A., Rocken, C., et al. (1996). The promise of GPS in atmospheric monitoring. *Bulletin of the American Meteorological Society*, *77*(1), 5–18. doi:10.1175/1520-0477(1996)077<0005:TPOGIA>2.0.CO;2.

Byun, S. H., & Bar-Sever, Y. E. (2009). A new type of troposphere zenith path delay product of the international GNSS service. *Journal of Geodesy*, *83*(3–4), 367–373. doi:10.1007/s00190-008-0288-8.

Cocard, M., Bourgon, S., Kamali, O., & Collins, P. (2008). A systematic investigation of optimal carrier-phase combinations for modernized triple-frequency GPS. *Journal of Geodesy*, *82*(9), 555–564. doi:10.1007/s00190-007-0201-x.

Collins, J. P. (1999). An overview of GPS inter-frequency carrier phase combinations. Geodetic Survey Division, Technical Memorandum, University of New Brunswick (UNB), New Brunswick.

Collins, P. (2008). Isolating and estimating undifferenced GPS integer ambiguities. In: *Proceedings of ION NTM 2008*, San Diego, CA, 28–30 Jan, pp. 720–732.

Czopek, F. M., & Shollenberger, S. (1993). Description and performance of the GPS Block I and II L-Band antenna and link budget. In: *Proceedings of ION GPS 1993*, Salt Lake City, UT, 22–24 Sep, pp. 37–43.

Dach, R., Hugentobler, U., Fridez, P., & Meindl, M. (2007). Bernese GPS Software Version 5.0. Astronomical Institute, University of Bern, Stämpfli Publications AG, Bern.

Dach, R., Böhm, J., Lutz, S., Steigenberger, P., & Beutler, G. (2010). Evaluation of the impact of atmospheric pressure loading modeling on GNSS data analysis. *Journal of Geodesy*, *85*(2), 75–91. doi:10.1007/s00190-010-0417-z.

Dach, R., Schmid, R., Schmitz, M., Thaller, D., Schaer, S., Lutz, S., et al. (2011). Improved antenna phase center models for GLONASS. *GPS Solutions*, *15*(1), 49–65. doi:10.1007/s10291-010-0169-5.

Dai, L., Han, S., Wang, J., & Rizos, C. (2001). A study on GPS/GLONASS multiple reference station techniques for precise real-time carrier phase-based positioning. In: *Proceedings of ION GPS 2001*, Salt Lake City, UT, 11–14 Sep, pp. 392–403.

Davis, J. L., Herring, T. A., Shapiro, I. I., Rogers, A. E. E., & Elgered, G. (1985). Geodesy by radio interferometry: Effects of atmospheric modeling errors on estimates of baseline length. *Radio Science*, *20*(6), 1593–1607. doi:10.1029/RS020i006p01593.

De Jonge, P. J., Teunissen, P. J. G., Jonkman, N. F., & Joosten, P. (2000). The distributional dependence of the range on triple frequency GPS ambiguity resolution. In: *Proceedings of ION NTM 2000*, Anaheim, CA, 26–28 Jan, pp. 605–612.

Dilßner, F. (2007). Zum Einfluss des Antennenumfeldes auf die hochpräzise GNSS-Positionsbestimmung. Wissenschaftliche Arbeiten der Fachrichtung Geodäsie und Geoinformatik der Leibniz Universität Hannover, No. 271, Hannover.

Dixon, K. (2005). Satellite positioning systems: Efficiencies, performance and trends. *European Journal of Navigation*, *3*(1), 58–63.

Dixon, K. (2006). StarFire: A global SBAS for sub-decimeter precise point positioning. In: *Proceedings of ION GNSS 2006*, Fort Worth, TX, 26–29 Sep, pp. 2286–2296.

Dragert, H., James, T. S., & Lambert, A. (2000). Ocean loading corrections for continuous GPS: A case study at the Canadian coastal site Holberg. *Geophysical Research Letters*, *27*(14), 2045–2048. doi:10.1029/2000GL011536.

El-Rabbany, A. (1994). The effect of physical correlations on the ambiguity resolution and accuracy estimation in GPS differential positioning. PhD thesis, Department of Geodesy and Geomatics Engineering, Technical Report, No. 170, University of New Brunswick (UNB), New Brunswick.

El-Rabbany, A. (2006). *Introduction to GPS: The Global Positioning System* (2nd ed.). Norwood: Artech House.

Elsobeiey, M., & El-Rabbany, A. (2011). Impact of second-order ionospheric delay on GPS precise point positioning. *Journal of Applied Geodesy*, *5*(1), 37–45. doi:10.1515/JAG.2011.004.

Euler, H.-J., & Goad, C. C. (1991). On optimal filtering of GPS dual frequency observations without using orbit information. *Bulletin Géodésique*, *65*(2), 130–143. doi:10.1007/BF00806368.

Fan, K. K., & Ding, X. L. (2006). Estimation of GPS carrier phase multipath signals based on site environment. *Journal of Global Positioning Systems*, *5*(1–2), 22–28.

Farrell, W. E. (1972). Deformation of the Earth by surface loads. *Reviews of Geophysics*, *10*(3), 761–797. doi:10.1029/RG010i003p00761.

Feng, Y. (2008). GNSS three carrier ambiguity resolution using ionosphere-reduced virtual signals. *Journal of Geodesy*, *82*(12), 847–862. doi:10.1007/s00190-008-0209-x.

Fontana, R. D., Cheung, W., Novak, P. M., & Stansell, T. A. (2001). The new L2 civil signal. In: *Proceedings of ION GPS 2001*, Salt Lake City, UT, 11–14 Sep, pp. 617–631.

Forssell, B., Martin-Neira, M., & Harrisz, R. A. (1997). Carrier phase ambiguity resolution in GNSS-2. In: *Proceedings of ION GPS 1997*, Kansas City, MO, 16–19 Sep, pp. 1727–1736.

Fotopoulos, G., & Cannon, M. E. (2001). An overview of multiple-reference station methods for cm-level positioning. *GPS Solutions*, *4*(3), 1–10. doi:10.1007/PL00012849.

Fritsche, M., Dietrich, R., Knöfel, C., Rülke, A., Vey, S., Rothacher, M., et al. (2005). Impact of higher-order ionospheric terms on GPS estimates. *Geophysical Research Letters*, *32*, L23311. doi:10.1029/2005GL024342.

Fuhrmann, T., Knöpfler, A., Mayer, M., Luo, X., & Heck, B. (2010). Zur GNSS-basierten Bestimmung des atmosphärischen Wasserdampfgehalts mittels Precise Point Positioning. Schriftenreihe des Studiengangs Geodäsie und Geoinformatik, Band 2/2010, Karlsruher Institut für Technologie (KIT), KIT Scientific Publishing, Karlsruhe.

Gao, Y., & Chen, K. (2004). Performance analysis of precise point positioning using real-time orbit and clock products. *Journal of Global Positioning Systems*, *3*(1–2), 95–100.

Ge, L., Han, S., & Rizos, C. (2000). Multipath mitigation of continuous GPS measurements using an adaptive filter. *GPS Solutions*, *4*(2), 19–30. doi:10.1007/PL00012838.

Ge, M., Gendt, G., Rothacher, M., Shi, C., & Liu, J. (2008). Resolution of GPS carrier-phase ambiguities in precise point positioning (PPP) with daily observations. *Journal of Geodesy*, *82*(7), 389–399. doi:10.1007/s00190-007-0187-4.

Geng, J., Teferle, F. N., Shi, C., Meng, X., Dodson, A. H., & Liu, J. (2009). Ambiguity resolution in precise point positioning with hourly data. *GPS Solutions*, *13*(4), 263–270. doi:10.1007/s10291-009-0119-2.

Geng, J., Meng, X., Teferle, F. N., & Dodson, A. H. (2010). Performance of precise point positioning with ambiguity resolution for 1–4 h observation periods. *Survey Review*, *42*(316), 155–165. doi:10.1179/003962610X12572516251682.

Ghoddousi-Fard, R., & Dare, P. (2006). Online GPS processing services: An initial study. *GPS Solutions*, *10*(1), 12–20. doi:10.1007/s10291-005-0147-5.

Görres, B., Campbell, J., Becker, M., & Siemes, M. (2006). Absolute calibration of GPS antennas: Laboratory results and comparison with field and robot techniques. *GPS Solutions*, *10*(2), 136–145. doi:10.1007/s10291-005-0015-3.

Görres, B. (2010a). Ist das GNSS-Antennenproblem gelöst? *Zeitschrift für Geodäsie, Geoinformation und Landmanagement (ZfV)*, *135*(4), 256–267.

Görres, B. (2010b). Vom globalen Bezugssystem bis zur Umsetzung für die Praxis. In: GNSS 2010—Vermessung und Navigation im 21. Jahrhundert, 100. DVW-Seminar, Köln, 4–5 Okt, DVW-Schriftenreihe, Band 63/2010, Augsburg: Wißner, pp. 39–56.

Guier, W. H., & Weiffenbach, G. C. (1997). Genesis of satellite navigation. *Johns Hopkins APL Technical Digest*, *18*(2), 178–181.

Han, S. (1997). Quality-control issues relating to instantaneous ambiguity resolution for real-time GPS kinematic positioning. *Journal of Geodesy*, *71*(6), 351–361. doi:10.1007/s001900050103.

Han, S., & Rizos, C. (1999). The impact of two additional civilian GPS frequencies on ambiguity resolution strategies. In: *Proceedings of the* 55*th Annual Meeting of The Institute of Navigation*, Cambridge, MA, 27–30 June, 1999, pp. 315–321.

Hatch, R., Jung, J., Enge, P., & Pervan, B. (2000). Civilian GPS: The benefits of three frequencies. *GPS Solutions*, *3*(4), 1–9. doi:10.1007/PL00012810.

Hein, G. W., Ávila-Rodríguez, J.-Á., & Wallner, S. (2006). The DaVinci Galileo code and others. *Inside GNSS*, *1*(6), 62–74.

Heister, H., Heunecke, O., Kerraschk, T., & Pflugmacher, A. (2009). Untersuchungen zu den globalen Positionierungsdiensten von Fugro OmniSTAR - Teil I: Grundlagen und Überblick. *Zeitschrift für Geodäsie, Geoinformation und Landmanagement* (*ZfV*), *134*(3), 131–140.

Heister, H., Heunecke, O., Kerraschk, T., & Pflugmacher, A. (2010). Untersuchungen zu den globalen Positionierungsdiensten von Fugro OmniSTAR - Teil II: Ergebnisse und Erfahrungen. *Zeitschrift für Geodäsie, Geoinformation und Landmanagement* (*ZfV*), *135*(1), 21–31.

Hernández-Pajares, M., Juan, J. M., Sanz, J., & Orúz, R. (2007). Second-order ionospheric term in GPS: Implementation and impact on geodetic estimates. *Journal of Geophysical Research*, *112*, B08417. doi:10.1029/2006JB004707.

Héroux, P., & Kouba, J. (2001). GPS precise point positioning using IGS orbit products. *Physics and Chemistry of the Earth, Part A: Solid Earth and Geodesy*, *26*(6–8), 573–578. doi:10.1016/S1464-1895(01)00103-X.

Herring, T. A. (1992). Modeling atmospheric delays in the analysis of space geodetic data. In: J. C. de Munck & T. A. Th. Spoelstra (Eds.), *Proceedings of the Symposium on Refraction of Transatmospheric Signals in Geodesy*, Hague, The Netherlands, 19–22 May, 1992, Netherlands Geodetic Commission, Delft, pp. 157–164.

Heßelbarth, A., & Wanninger, L. (2008). Short-term stability of GNSS satellite clocks and its effects on precise point positioning. In: *Proceedings of ION GNSS 2008*, Savannah, GA, 16–19 Sep, pp. 1855–1863.

Heßelbarth, A. (2009). GNSS-Auswertung mittels Precise Point Positioning (PPP). *Zeitschrift für Geodäsie, Geoinformation und Landmanagement* (*ZfV*), *134*(5), 278–286.

Heunecke, O., & Heister, H. (2010). Untersuchungen zur Genauigkeit und Verfügbarkeit der Korrekturdienste von Fugro OmniSTAR. In: GNSS 2010—Vermessung und Navigation im 21. Jahrhundert, 100. DVW-Seminar, Köln, 4–5 Okt, DVW-Schriftenreihe, Band 63/2010, Augsburg: Wißner, pp. 143–160.

Hofmann-Wellenhof, B., Lichtenegger, H., & Wasle, E. (2008). *GNSS-Global Navigation Satellite Systems: GPS, GLONASS, Galileo & more*. Wien: Springer.
Hopfield, H. S. (1969). Two-quartic tropospheric refractivity profile for correcting satellite data. *Journal of Geophysical Research*, *74*(18), 4487–4499. doi:10.1029/JC074i018p04487.
Howind, J., Kutterer, H., & Heck, B. (1999). Impact of temporal correlations on GPS-derived relative point positions. *Journal of Geodesy*, *73*(5), 246–258. doi:10.1007/s001900050241.
Howind, J. (2005). Analyse des stochastischen Modells von GPS-Trägerphasenbeobachtungen. Deutsche Geodätische Kommission, No. C584, Verlag der Bayerischen Akademie der Wissenschaften, Munich.
ICD-GPS-200C (1993). Interface Control Document: NAVSTAR GPS space segment/navigation user interfaces, ICD-GPS-200, Revision C. ARINC Research Corporation, El Segundo, CA, 10 Oct.
Jin, S. G., & Park, P. H. (2005). A new precision improvement in zenith tropospheric delay estimation by GPS. *Current Science*, *89*(6), 997–1000.
Jin, S. G., Wang, J., & Park, P. H. (2005). An improvement of GPS height estimations: Stochastic modeling. *Earth, Planets and Space*, *57*(4), 253–259.
Kaniuth, K., & Vetter, S. (2006). Estimating atmospheric pressure loading regression coefficients from GPS observations. *GPS Solutions*, *10*(2), 126–134. doi:10.1007/s10291-005-0014-4.
Kaplan, E. D., & Hegarty, C. J. (2006). *Understanding GPS: Principles and applications* (2nd ed.). Norwood: Artech House.
Karabatić, A. (2011). Precise Point Positioning (PPP)–An alternative technique for ground based GNSS troposphere monitoring. Geowissenschaftliche Mitteilungen, No. 86, Vienna University of Technology, Vienna.
Kechine, M. O., Tiberius, C. C. J. M., & van der Marel, H. (2003). Network differential GPS: Kinematic positioning with NASA's Internet-based global differential GPS. *Journal of Global Positioning Systems*, *2*(2), 139–143.
Kedar, S., Hajj, G. A., Wilson, B. D., & Heflin, M. B. (2003). The effect of the second-order GPS ionospheric correction on receiver positions. *Geophysical Research Letters*, *30*(16), 1829. doi:10.1029/2003GL017639.
Kee, C. (1996). Wide area differential GPS. In: B. W. Parkinson & J. J. Spilker (Eds.), *Global Positioning System: Theory and applications*, vol. 2, American Institute of Aeronautics and Astronautics, Washington D.C., pp. 81–115.
Kelly, J. T. (2006). PPS versus SPS: Why military applications require military GPS. *GPS World*, *17*(1), 28–35.
Kim, D., & Langley, R. B. (2001). Quality control techniques and issues in GPS applications: Stochastic modelling and reliability testing. In: *Proceedings of the 8th GNSS Workshop—2001 International Symposium on GPS/GNSS*, Jeju, Korea, Tutorial/Domestic Session, 7–9 Nov, pp. 76–85.
King, R. W., & Bock, Y. (2002). Documentation for the GAMIT GPS Analysis Software, Release 10.0. Massachusetts Institute of Technology (MIT), Cambridge.
Kouba, J., & Héroux, P. (2001). Precise point positioning using IGS orbit and clock products. *GPS Solutions*, *5*(2), 12–28. doi:10.1007/PL00012883.
Kouba, J. (2002a). Relativistic time transformations in GPS. *GPS Solutions*, *5*(4), 1–9. doi:10.1007/PL00012907.
Kouba, J. (2002b). Sub-daily Earth rotation parameters and the International GPS Service orbit/clock solution products. *Studia Geophysica et Geodaetica*, *46*(1), 9–25. doi:10.1023/A:1019894614643.
Kouba, J. (2004). Improved relativistic transformations in GPS. *GPS Solutions*, *8*(3), 170–180. doi:10.1007/s10291-004-0102-x.
Kouba, J. (2009). A guide to using International GNSS Service (IGS) products. Available online at http://igscb.jpl.nasa.gov/igscb/resource/pubs/UsingIGSProductsVer21.pdf, accessed on 5 Nov, 2010.
Langley, R. B. (1991a). The mathematics of GPS. *GPS World*, *2*(7), 45–50.
Langley, R. B. (1991b). The orbits of GPS satellites. *GPS World*, *2*(3), 50–53.

Langley, R. B. (1997). GPS receiver system noise. *GPS World*, *8*(6), 40–45.
Lau, L. (2012). Comparison of measurement and position domain multipath filtering techniques with the repeatable GPS orbits for static antennas. *Survey Review*, *44*(324), 9–16. doi:10.1179/1752270611Y.0000000003.
Laurichesse, D., & Mercier, F. (2007). Integer ambiguity resolution on undifferenced GPS phase measurements and its application to PPP. In: *Proceedings of ION GNSS 2007*, Fort Worth, TX, 25–28 Sep, pp. 839–848.
Le, A. Q., & Tiberius, C. C. J. M. (2006). Phase wind-up effects in precise point positioning with kinematic platforms. In: *Proceedings of the 3rd ESA Workshop on Satellite Navigation User Equipment Technologies*, Noordwijk, The Netherlands, 11–13 Dec.
Leandro, R. F., & Santos, M. C. (2007). Stochastic models for GPS positioning: An empirical approach. *GPS World*, *18*(2), 50–56.
Leick, A. (1995). *GPS satellite surveying* (2nd ed.). New York: Wiley.
Leick, A. (2003). *GPS satellite surveying* (3rd ed.). Hoboken: Wiley.
Li, B., Shen, Y., & Xu, P. (2008). Assessment of stochastic models for GPS measurements with different types of receivers. *Chinese Science Bulletin*, *53*(20), 3219–3225. doi:10.1007/s11434-008-0293-6.
Li, B., Shen, Y., & Lou, L. (2011). Efficient estimation of variance and covariance components: A case study for GPS stochastic model evaluation. *IEEE Transactions on Geoscience and Remote Sensing*, *49*(1), 203–210. doi:10.1109/TGRS.2010.2054100.
Liu, H., Li, X., Ge, L., Rizos, C., & Wang, F. (2011). Variable length LMS adaptive filter for carrier phase multipath mitigation. *GPS Solutions*, *15*(1), 29–38. doi:10.1007/s10291-010-0165-9.
Luo, X., Mayer, M., & Heck, B. (2007a). Bestimmung von hochauflösenden Wasserdampffeldern unter Berücksichtigung von GNSS-Doppeldifferenzresiduen. Schriftenreihe des Studiengangs Geodäsie und Geoinformatik, Band 2/2007, Karlsruher Institut für Technologie (KIT), KIT Scientific Publishing, Karlsruhe.
Luo, X., Mayer, M., & Heck, B. (2007b). Erweiterte Modellbildung zur Erzeugung von hochauflösenden Wasserdampffeldern. *Allgemeine Vermessungs-Nachrichten (AVN)*, *114*(5), 179–189.
Luo, X., Mayer, M., & Heck, B. (2007c). Quantifizierung verschiedener Einflussfaktoren in GNSS-Residuen. *Zeitschrift für Geodäsie, Geoinformation und Landmanagement* (*ZfV*), 132(2), 97–107.
Luo, X., Mayer, M., & Heck, B. (2008a). Erweiterung des stochastischen Modells von GNSS-Beobachtungen unter Verwendung der Signalqualität. *Zeitschrift für Geodäsie, Geoinformation und Landmanagement* (*ZfV*), *133*(2), 98–107.
Luo, X., Mayer, M., & Heck, B. (2008b). Extended neutrospheric modelling for the GNSS-based determination of high-resolution atmospheric water vapour fields. *Boletim de Ciências Geodésicas*, *14*(2), 149–170.
Luo, X., Mayer, M., & Heck, B. (2008c). Impact of various factors on the quality of site-specific neutrospheric parameters within GNSS data processing: A case study. *Boletim de Ciências Geodésicas*, *14*(4), 461–481.
Luo, X., Mayer, M., & Heck, B. (2008d). Improving the stochastic model of GNSS observations by means of SNR-based weighting. In: M. G. Sideris (Ed.), *Observing our changing Earth, Proceedings of the 2007 IAG General Assembly*, Perugia, Italy, 2–13 July, IAG Symposia, vol. 133, Berlin: Springer, pp. 725–734. doi:10.1007/978-3-540-85426-5_83.
Luo, X., Heck, B., & Awange, J. L. (2012a). Improving the estimation of zenith dry tropospheric delays using regional surface meteorological data. *Advances in Space Research* (submitted).
Luo, X., Mayer, M., & Heck, B. (2012b). Analysing time series of GNSS residuals by means of AR(I)MA processes. In: N. Sneeuw et al. (Eds.), *Proceedings of the VII Hotine-Marussi Symposium on Mathematical Geodesy*, Rome, Italy, 6–10 July, 2009, IAG Symposia, vol. 137, Berlin: Springer, pp. 129–134. doi:10.1007/978-3-642-22078-4_19.
Lutz, S. (2009). High-resolution GPS tomography in view of hydrological hazard assessment. Geodätisch-geophysikalische Arbeiten in der Schweiz, No. 76, Schweizerische Geodätische Kommission, Zurich.

Mader, G. L. (1999). GPS antenna calibration at the National Geodetic Survey. *GPS Solutions*, *3*(1), 50–58. doi:10.1007/PL00012780.
Mader, G. L. (2001). A comparison of absolute and relative GPS antenna calibrations. *GPS Solutions*, *4*(4), 37–40. doi:10.1007/PL00012864.
Mangiarotti, S., Cazenave, A., Soudarin, L., & Crétaux, J. F. (2001). Annual vertical crustal motions predicted from surface mass redistribution and observed by space geodesy. *Journal of Geophysical Research*, *106*(B3), 4277–4291. doi:10.1029/2000JB900347.
Marini, J. W. (1972). Correction of satellite tracking data for an arbitrary tropospheric profile. *Radio Science*, *7*(2), 223–231. doi:10.1029/RS007i002p00223.
Marmet, P. (2000). The GPS and the constant velocity of light. *Acta Scientiarum. Technology*, *22*(5), 1269–1279.
Marquis, W., & Riggs, J. D. (2010). Block IIR lifetimes and GPS sustainment. *GPS World*, *21*(11), 8–15.
Mathews, P. M., Dehant, V., & Gipson, J. M. (1997). Tidal station displacements. *Journal of Geophysical Research*, *102*(B9), 20469–20477. doi:10.1029/97JB01515.
McCarthy, D. D., & Petit, G. (2004). IERS Conventions (2003). IERS Technical Note, No. 32, Verlag des Bundesamts für Kartographie und Geodäsie, Frankfurt am Main.
Meindl, M., Schaer, S., Hugentobler, U., & Beutler, G. (2004). Tropospheric gradient estimation at CODE: Results from global solutions. *Journal of the Meteorological Society of Japan*, *82*(1B), 331–338. doi:10.2151/jmsj.2004.331.
Melbourne, W. G. (1985). The case for ranging in GPS based geodetic systems. In: C. Goad (Ed.), *Proceedings of the* 1*st International Symposium on Precise Positioning with the Global Positioning System*, Rockville, MD, 15–19 Apr, 1985, pp. 373–386.
Menge, F., Seeber, G., Völksen, C., Wübbena, G., & Schmitz, M. (1998). Results of absolute field calibration of GPS antenna PCV. In: *Proceedings of ION GPS 1998*, Nashville, TN, 15–18 Sep, pp. 31–38.
Merrigan, M. J., Swift, E. R., Wong, R. F., & Saffel, J. T. (2002). A refinement to the World Geodetic System 1984 reference frame. In: *Proceedings of ION GPS 2002*, Portland, OR, 24–27 Sep, pp. 1519–1529.
Mireault, Y., Tétreault, P., Lahaye, F., Héroux, P., & Kouba, J. (2008). Online precise point positioning: A new, timely service from Natural Resources Canada. *GPS World*, *19*(9), 59–64.
Moore, A. W. (2007). The International GNSS Service: Any questions? *GPS World*, *18*(1), 58–64.
Morland, J., & Mätzler, C. (2007). Spatial interpolation of GPS integrated water vapour measurements made in the Swiss Alps. *Meteorological Applications*, *14*(1), 15–26. doi:10.1002/met.2.
Mueller, T. M. (1994). Wide area differential GPS. *GPS World*, *5*(6), 36–44.
Mungan, C. E. (2006). Relativistic effects on clocks aboard GPS satellites. *The Physics Teacher*, *44*(7), 424–425. doi:10.1119/1.2353579.
Nahavandchi, H., & Joodaki, G. (2010). Correlation analysis of multipath effects in GPS-code and carrier phase observations. *Survey Review*, *42*(316), 193–206. doi:10.1179/003962610X12572516251808.
Newby, S. P. (1992). An assessment of empirical models for the prediction of the transionospheric propagation delay of radio signals. M.Sc.E. thesis, Department of Surveying and Engineering, Technical Report, No. 160, University of New Brunswick (UNB), New Brunswick.
Niell, A. E. (1996). Global mapping functions for the atmosphere delay at radio wavelengths. *Journal of Geophysical Research*, *101*(B2), 3227–3246. doi:10.1029/95JB03048.
Niell, A. E. (2000). Improved atmospheric mapping functions for VLBI and GPS. *Earth, Planets and Space*, *52*(10), 699–702.
Niell, A. E. (2001). Preliminary evaluation of atmospheric mapping functions based on numerical weather models. *Physics and Chemistry of the Earth, Part A: Solid Earth and Geodesy*, *26*(6–8), 475–480. doi:10.1016/S1464-1895(01)00087-4.
NOAA/NASA/USAF (1976). U.S. Standard Atmosphere (1976). NOAA–S/T 76–1562, U.S. Government Printing Office, Washington D.C.

Odijk, D. (2003). Ionosphere-free phase combinations for modernized GPS. *Journal of Surveying Engineering*, *129*(4), 165–173. doi:10.1061/(ASCE)0733-9453(2003)129:4(165).
Parkinson, B. W., & Powers, S. T. (2010). The origins of GPS and the pioneers who launched the system. *GPS World*, *21*(5), 31–41.
Petit, G., & Luzum, B. (2010). IERS Conventions (2010). IERS Technical Note, No. 36, Verlag des Bundesamts für Kartographie und Geodäsie, Frankfurt am Main.
Petrov, L., & Boy, J.-P. (2004). Study of the atmospheric pressure loading signal in very long baseline interferometry observations. *Journal of Geophysical Research*, *109*, B03405. doi:10.1029/2003JB002500.
Pireaux, S., Defraigne, P., Wauters, L., Bergeot, N., Baire, Q., & Bruyninx, C. (2010). Higher-order ionospheric effects in GPS time and frequency transfer. *GPS Solutions*, *14*(3), 267–277. doi:10.1007/s10291-009-0152-1.
Prasad, R., & Ruggieri, M. (2005). *Applied satellite navigation using GPS, GALILEO, and augmentation systems*. Norwood: Artech House.
Ragheb, A. E., Clarke, P. J., & Edwards, S. J. (2007). GPS sidereal filtering: Coordinate- and carrier-phase-level strategies. *Journal of Geodesy*, *81*(5), 325–335. doi:10.1007/s00190-006-0113-1.
Rao, C. R. (1970). Estimation of heteroscedastic variances in linear models. *Journal of the American Statistical Association*, *65*(329), 161–172. doi:10.2307/2283583.
Rao, C. R. (1971). Estimation of variance and covariance components–MINQUE theory. *Journal of Multivariate Analysis*, *1*(3), 257–275. doi:10.1016/0047-259X(71)90001-7.
Ray, J. (2006). GNSS solutions: What receiver technologies exist for mitigating GNSS pseudorange and carrier phase multipath? *Inside GNSS*, *1*(6), 25–27.
Ray, J., & Griffiths, J. (2008). Overview of IGS products and analysis center modeling. Paper preseted at the IGS Analysis Center Workshop 2008, Miami Beach, FL, 2–6 June.
Rideout, W., & Coster, A. (2006). Automated GPS processing for global total electron content data. *GPS Solutions*, *10*(3), 219–228. doi:10.1007/s10291-006-0029-5.
Rizos, C. (2003). Network RTK research and implementation–A geodetic perspective. *Journal of Global Positioning Systems*, *1*(2), 144–150.
Rodrigues, E. P. (2007). Estimation of crustal vertical movements due to atmospheric loading effects by GPS observations. *Revista Brasileira de Geofísica*, *25*(1), 45–50. doi:10.1590/S0102-261X2007000100004.
Rost, C., & Wanninger, L. (2009). Carrier phase multipath mitigation based on GNSS signal quality measurements. *Journal of Applied Geodesy*, *3*(2), 81–87. doi:10.1515/JAG.2009.009.
Rost, C. & Wanninger, L. (2010). Carrier phase multipath corrections based on GNSS signal quality measurements to improve CORS observations. In: *Proceedings of IEEE/ION PLANS 2010*, Indian Wells, CA, 4–6 May, pp. 1162–1167.
Rost, C. (2011). Phasenmehrwegereduzierung basierend auf Signalqualitätsmessungen geodätischer GNSS-Empfänger. Deutsche Geodätische Kommission, No. C665, Verlag der Bayerischen Akademie der Wissenschaften, Munich.
Rothacher, M. (1992). Orbits of satellite systems in space geodesy. Geodätisch-geophysikalische Arbeiten in der Schweiz, No. 46, Schweizerische Geodätische Kommission, Zurich.
Rothacher, M. (2001). Comparison of absolute and relative antenna phase center variations. *GPS Solutions*, *4*(4), 55–60. doi:10.1007/PL00012867.
Saha, K., Raju, C. S., & Parameswaran, K. (2010). A new hydrostatic mapping function for tropospheric delay estimation. *Journal of Atmospheric and Solar-Terrestrial Physics*, *72*(1), 125–134. doi:10.1016/j.jastp.2009.10.017.
Santerre, R. (1989). GPS satellite sky distribution: Impact on the propagation of some important errors in precise relative positioning. PhD thesis, Department of Surveying Engineering, Technical Report, No. 145, University of New Brunswick (UNB), New Brunswick.
Santos, M. C., Vaníček, P., & Langley, R. B. (1997). Effect of mathematical correlation on GPS network computation. *Journal of Surveying Engineering*, *123*(3), 101–112. doi:10.1061/(ASCE)0733-9453(1997)123:3(101).

Satirapod, C., Wang, J., & Rizos, C. (2002). A simplified MINQUE procedure for the estimation of variance-covariance components of GPS observables. *Survey Review*, *36*(286), 582–590. doi:10.1179/003962602791482920.

Satirapod, C., & Rizos, C. (2005). Multipath mitigation by wavelet analysis for GPS base station applications. *Survey Review*, *38*(295), 2–10. doi:10.1179/003962605791521699.

Satirapod, C., & Luansang, M. (2008). Comparing stochastic model used in GPS precise point positioning technique. *Survey Review*, *40*(308), 188–194. doi:10.1179/003962608X290988.

Schmid, R., & Rothacher, M. (2003). Estimation of elevation-dependent satellite antenna phase center variations of GPS satellites. *Journal of Geodesy*, *77*(7–8), 440–446. doi:10.1007/s00190-003-0339-0.

Schmid, R., Rothacher, M., Thaller, D., & Steigenberger, P. (2005). Absolute phase center corrections of satellite and receiver antennas: Impact on global GPS solutions and estimation of azimuthal phase center variations of the satellite antenna. *GPS Solutions*, *9*(4), 283–293. doi:10.1007/s10291-005-0134-x.

Schmid, R., Steigenberger, P., Gendt, G., Ge, M., & Rothacher, M. (2007). Generation of a consistent absolute phase-center correction model for GPS receiver and satellite antennas. *Journal of Geodesy*, *81*(12), 781–798. doi:10.1007/s00190-007-0148-y.

Schmid, R. (2010). How to use IGS antenna phase center corrections. GPS World Tech Talk Blog, 3 Feb, 2010.

Schön, S., & Brunner, F. K. (2008a). Atmospheric turbulence theory applied to GPS carrier-phase data. *Journal of Geodesy*, *82*(1), 47–57. doi:10.1007/s00190-007-0156-y.

Schön, S., & Brunner, F. K. (2008b). A proposal for modelling physical correlations of GPS phase observations. *Journal of Geodesy*, *82*(10), 601–612. doi:10.1007/s00190-008-0211-3.

Schön, S. (2010). Differentielle GNSS Systeme–Code- und Phasenlösungen. In: GNSS 2010—Vermessung und Navigation im 21. Jahrhundert, 100. DVW-Seminar, Köln, 4–5 Okt, DVW-Schriftenreihe, Band 63/2010, Augsburg: Wißner, pp. 15–38.

Schuh, H., Estermann, G., Crétaux, J.-F., Bergé-Nguyen, M., & van Dam, T. (2004). Investigation of hydrological and atmospheric loading by space geodetic techniques. In: C. Hwang et al. (Eds.), *Satellite altimetry for geodesy, geophysics and oceanography, Proceedings of the International Workshop on Satellite Altimetry*, Wuhan, China, 8–13 Sep, 2002, IAG Symposia, vol. 126, Berlin: Springer, pp. 123–132. doi:10.1007/978-3-642-18861-9_15.

Seeber, G. (2003). *Satellite geodesy* (2nd ed.). Berlin: Walter de Gruyter.

Souza, E. M., & Monico, J. F. G. (2004). Wavelet shrinkage: High frequency multipath reduction from GPS relative positioning. *GPS Solutions*, *8*(3), 152–159. doi:10.1007/s10291-004-0100-z.

Springer, T., & Dach, R. (2010). GPS, GLONASS, and more: Multiple constellation processing in the International GNSS Service. *GPS World*, *21*(6), 48–58.

Steigenberger, P. (2009). Reprocessing of a global GPS network. Deutsche Geodätische Kommission, No. C640, Verlag der Bayerischen Akademie der Wissenschaften, Munich.

Steigenberger, P., Boehm, J., & Tesmer, V. (2009). Comparison of GMF/GPT with VMF1/ECMWF and implications for atmospheric loading. *Journal of Geodesy*, *83*(10), 943–951. doi:10.1007/s00190-009-0311-8.

Stronk, M., & Wegener, V. (2005). A satellite positioning service of the German State Survey. *GeoInformatics*, *8*, 40–43.

Sun, H.-P., Ducarme, B., & Dehant, V. (1995). Effect of the atmospheric pressure on surface displacements. *Journal of Geodesy*, *70*(3), 131–139. doi:10.1007/BF00943688.

Tetewsky, A. K., & Mullen, F. E. (1997). Carrier phase wrap-up induced by rotating GPS antennas. *GPS World*, *8*(2), 51–57.

Tétreault, P., Kouba, J., Héroux, P., & Legree, P. (2005). CSRS-PPP: An internet service for GPS user access to the Canadian Spatial Reference Frame. *Geomatica*, *59*(1), 17–28.

Teunissen, P. J. G. (1995). The least-squares ambiguity decorrelation adjustment: A method for fast GPS integer ambiguity estimation. *Journal of Geodesy*, *70*(1–2), 65–82. doi:10.1007/BF00863419.

Teunissen, P. J. G. (1998). Quality control and GPS. In: P. J. G. Teunissen & A. Kleusberg (Eds.), *GPS for geodesy* (2nd ed.), chapter 7, Berlin: Springer.

Teunissen, P. J. G., & Kleusberg, A. (1998). *GPS for geodesy* (2nd ed.). Berlin: Springer.

Teunissen, P. J. G., Jonkman, N. F., & Tiberius, C. C. J. M. (1998). Weighting GPS dual frequency observations: Bearing the cross of cross-correlation. *GPS Solutions*, *2*(2), 28–37. doi:10.1007/PL00000033.

Teunissen, P. J. G. (2000). The success rate and precision of GPS ambiguities. *Journal of Geodesy*, *74*(3–4), 321–326. doi:10.1007/s001900050289.

Teunissen, P., Joosten, P., & Tiberius, C. (2002). A comparison of TCAR, CIR and LAMBDA GNSS ambiguity resolution. In: *Proceedings of ION GPS 2002*, Portland, OR, 24–27 Sep, pp. 2799–2808.

Tiberius, C., Jonkman, N., & Kenselaar, F. (1999). The stochastics of GPS observables. *GPS World*, *10*(2), 49–54.

Tiberius, C., & Kenselaar, F. (2003). Variance component estimation and precise GPS positioning: Case study. *Journal of Surveying Engineering*, *129*(1), 11–18. doi:10.1061/(ASCE)0733-9453(2003)129:1(11).

Torge, W. (2001). *Geodesy* (3rd ed.). Berlin: Walter de Gruyter.

Tregoning, P., & van Dam, T. (2005). Atmospheric pressure loading corrections applied to GPS data at the observation level. *Geophysical Research Letters*, *32*, L22310. doi:10.1029/2005GL024104.

Tregoning, P., Watson, C., Ramillien, G., McQueen, H., & Zhang, J. (2009). Detecting hydrologic deformation using GRACE and GPS. *Geophysical Research Letters*, *36*, L15401. doi:10.1029/2009GL038718.

Troller, M. (2004). GPS based determination of the integrated and spatially distributed water vapor in the troposphere. Geodätisch-geophysikalische Arbeiten in der Schweiz, No. 67, Schweizerische Geodätische Kommission, Zurich.

Troller, M., Geiger, A., Brockmann, E., & Kahle, H.-G. (2006). Determination of the spatial and temporal variation of tropospheric water vapour using CGPS networks. *Geophysical Journal International*, *167*(2), 509–520. doi:10.1111/j.1365-246X.2006.03101.x.

van Dam, T. M., Blewitt, G., & Heflin, M. B. (1994). Atmospheric pressure loading effects on Global Positioning System coordinate determinations. *Journal of Geophysical Research*, 99(B12), 23939–23950. doi:10.1029/94JB02122.

Vollath, U., Birnbach, S., Landau, H., Fraile-Ordoñez, J. M., & Martin-Neira, M. (1998). Analysis of three carrier ambiguity resolution (TCAR) technique for precise relative positioning in GNSS-2. In: *Proceedings of ION GPS 1998*, Nashville, TN, 15–18 Sep, pp. 417–426.

Wang, J., Stewart, M. P., & Tsakiri, M. (1998). Stochastic modeling for static GPS baseline data processing. *Journal of Surveying Engineering*, *124*(4), 171–181. doi:10.1061/(ASCE)0733-9453(1998)124:4(171).

Wang, J., Satirapod, C., & Rizos, C. (2002). Stochastic assessment of GPS carrier phase measurements for precise static relative positioning. *Journal of Geodesy*, *76*(2), 95–104. doi:10.1007/s00190-001-0225-6.

Wanninger, L. (2000). Präzise Positionierung in regionalen GPS-Referenzstationsnetzen. Deutsche Geodätische Kommission, No. C508, Verlag der Bayerischen Akademie der Wissenschaften, Munich.

Wanninger, L. (2002). Virtual reference stations for centimeter-level kinematic positioning. In: *Proceedings of ION GPS 2002*, Portland, OR, 24–27 Sep, pp. 1400–1407.

Wanninger, L. (2003). Virtual reference stations (VRS). *GPS Solutions*, *7*(2), 143–144. doi:10.1007/s10291-003-0060-8.

Wanninger, L. (2004). Introduction to network RTK. IAG Working Group 4.5.1: Network RTK (2003–2007), available online at www.wasoft.de/e/iagwg451/intro/introduction.html, accessed on 7 Sep, 2011.

Wanninger, L. (2006). Netz-RTK. In: GPS und Galileo—Methoden, Lösungen und neueste Entwicklungen, 66. DVW-Seminar, Darmstadt, 21–22 Feb, DVW-Schriftenreihe, Band 49/2006, Augsburg: Wißner, pp. 59–69.

Wanninger, L., & Heßelbarth, A. (2009). GNSS Precise Point Positioning und seine Anwendung in der Hydrographie. In: Hydrographie—Neue Methoden von der Erfassung zum Produkt, 89. DVW-Seminar, Hamburg, 6–7 Okt, DVW-Schriftenreihe, Band 58/2009, Augsburg: Wißner, pp. 3–18.

Ware, R., Alber, C., Rocken, C., & Solheim, F. (1997). Sensing integrated water vapor along GPS ray paths. *Geophysical Research Letters*, *24*(4), 417–420. doi:10.1029/97GL00080.

Watson, C., Tregoning, P., & Coleman, R. (2006). Impact of solid Earth tide models on GPS coordinate and tropospheric time series. *Geophysical Research Letters*, *33*, L08306. doi:10.1029/2005GL025538.

Weinbach, U., Raziq, N., & Collier, P. (2009). Mitigation of periodic GPS multipath errors using a normalised least mean square adaptive filter. *Journal of Spatial Science*, *54*(1), 1–13. doi:10.1080/14498596.2009.9635162.

Wieser, A., & Brunner, F. K. (2002). Short static GPS sessions: Robust estimation results. *GPS Solutions*, *5*(3), 70–79. doi:10.1007/PL00012901.

Wieser, A. (2007). GNSS solutions: How important is GNSS observation weighting? *Inside GNSS*, *2*(1), 26–28.

Wildt, S. (2007). Mehrwegeausbreitung bei GNSS-gestützter Positionsbestimmung. PhD thesis, Fakultät für Forst-, Geo- und Hydrowissenschaften der TU Dresden, Dresden.

Williams, S. D. P., & Penna, N. T. (2011). Non-tidal ocean loading effects on geodetic GPS heights. *Geophysical Research Letters*, *38*, L09314. doi:10.1029/2011GL046940.

Witchayangkoon, B. (2000). Elements of GPS Precise Point Positioning. PhD thesis, Department of Spatial Information Science and Engineering, University of Maine, Orono.

Woods, A. (2006). *Medium-range weather prediction: The European approach (The story of the European Centre for Medium-Range Weather Forecasts)*. New York: Springer.

Wu, J., Gao, J., Li, M., & Wang, Y. (2009). Wavelet transform for GPS carrier phase multipath mitigation. In: *Proceedings of the* 1*st International Conference on Information Science and Engineering*, Nanjing, China, 26–28 Dec, 2009, pp. 1019–1022. doi:10.1109/ICISE.2009.1344.

Wu, J. T., Wu, S. C., Hajj, G. A., Bertiger, W. I., & Lichten, S. M. (1993). Effects of antenna orientation on GPS carrier phase. *Manuscripta Geodetica*, *18*(2), 91–98.

Wübbena, G. (1985). Software developments for geodetic positioning with GPS using TI 4100 code and carrier measurements. In: C. Goad (Ed.), *Proceedings of the* 1*st International Symposium on Precise Positioning with the Global Positioning System*, Rockville, MD, 15–19 Apr, 1985, pp. 403–412.

Wübbena, G., Schmitz, M., Menge, F., Böder, V., & Seeber, G. (2000). Automated absolute field calibration of GPS antennas in real-time. In: *Proceedings of ION GPS 2000*, Salt Lake City, UT, 19–22 Sep, pp. 2512–2522.

Wübbena, G., Bagge, A., & Schmitz, M. (2001). Network-based techniques for RTK applications. In: *Proceedings of GPS JIN 2001, GPS Society, Japan Institute of Navigation*, Tokyo, Japan, 14–16 Nov, pp. 53–65.

Wübbena, G., Schmitz, M., & Bagge, A. (2005). PPP-RTK: Precise point positioning using state-space representation in RTK networks. In: *Proceedings of ION GNSS 2005*, Long Beach, CA, 13–16 Sep, pp. 2584–2594.

Wübbena, G., Schmitz, M., & Boettcher, G. (2006a). Near-field effects on GNSS sites: Analysis using absolute robot calibrations and procedures to determine corrections. In: *Proceedings of the IGS Workshop—Perspectives and Visions for* 2010 *and beyond*, 8–12 May, ESOC, Darmstadt.

Wübbena, G., Schmitz, M., Boettcher, G., & Schumann, C. (2006b). Absolute GNSS antenna calibration with a robot: Repeatability of phase variations, calibration of GLONASS and determination of carrier-to-noise pattern. In: *Proceedings of the IGS Workshop—Perspectives and Visions for* 2010 *and beyond*, 8–12 May, ESOC, Darmstadt.

Wübbena, G., Schmitz, M., & Matzke, N. (2011). On GNSS in-situ station calibration of near-field multipath. Paper submitted to the International Symposium on GNSS, Space-based and Ground-based Augmentation Systems and Applications, Brussels, Belgium, 29–30 Nov, 2010.

Xia, L., & Liu, J. (2001). Approach for multipath reduction using wavelet algorithm. In: *Proceedings of ION GPS 2001*, Salt Lake City, UT, 11–14 Sep, pp. 2134–2143.

Xu, G. (2007). *GPS: Theory, algorithms and applications* (2*nd* ed.). Berlin: Springer.

Zeimetz, P., & Kuhlmann, H. (2006). Systematic effects in absolute chamber calibration of GPS antennas. *Geomatica*, *60*(3), 267–274.

Zeimetz, P., & Kuhlmann, H. (2008). On the accuracy of absolute GNSS antenna calibration and the conception of a new anechoic chamber. In: *Proceedings of FIG Working Week 2008—Integrating Generations*, Stockholm, Sweden, 14–19 June.

Zheng, D. W., Zhong, P., Ding, X. L., & Chen, W. (2005). Filtering GPS time-series using a Vondrak filter and cross-validation. *Journal of Geodesy*, *79*(6–7), 363–369. doi:10.1007/s00190-005-0474-x.

Zhong, P., Ding, X. L., Zheng, D. W., Chen, W., & Huang, D. F. (2008). Adaptive wavelet transform based on cross-validation method and its application to GPS multipath mitigation. *GPS Solutions*, *12*(2), 109–117. doi:10.1007/s10291-007-0071-y.

Zhong, P., Ding, X., Yuan, L., Xu, Y., Kwok, K., & Chen, Y. (2010). Sidereal filtering based on single differences for mitigating GPS multipath effects on short baselines. *Journal of Geodesy*, *84*(2), 145–158. doi:10.1007/s00190-009-0352-z.

Zhu, S. Y., & Groten, E. (1988). Relativistic effects in GPS. In: E. Groten & R. Strauß (Eds.), *GPS-techniques applied to geodesy and surveying, Proceedings of the International GPS-Workshop*, Darmstadt, Germany, 10–13 Apr, 1988, Lectures Notes in Earth Sciences, vol. 19, Berlin: Springer, pp. 41–46. doi:10.1007/BFb0011322.

Zhu, S. Y., Massmann, F.-H., Yu, Y., & Reigber, Ch. (2003). Satellite antenna phase center offsets and scale errors in GPS solutions. *Journal of Geodesy*, *76*(11–12), 668–672. doi:10.1007/s00190-002-0294-1.

Zumberge, J. F., Heflin, M. B., Jefferson, D. C., Watkins, M. M., & Webb, F. H. (1997). Precise point positioning for the efficient and robust analysis of GPS data from large networks. *Journal of Geophysical Research*, *102*(B3), 5005–5017. doi:10.1029/96JB03860.